INTERNATIONAL JOURNAL FOR NUMERICAL METHODS IN FLUIDS
*Int. J. Numer. Meth. Fluids* 2007; **54**:419–451
Published online 21 December 2006 in Wiley InterScience (www.interscience.wiley.com). DOI: 10.1002/fld.1406

# Simulation of ship breaking bow waves and induced vortices and scars

Robert V. Wilson*, †, Pablo M. Carrica and Fred Stern

*IIHR - Hydroscience and Engineering, The University of Iowa, Iowa City, IA 52242, U.S.A.*

SUMMARY

An unsteady single-phase level set RANS method is used to resolve and investigate bow wave breaking around a surface combatant advancing in calm water, including induced vortices and free surface scars. A level set free surface capturing approach was extended and combined with local overset grid refinement for resolution of complex interfacial topologies and small-scale free surface features. Although the focus of the paper is on wave breaking at $Fr = 0.35$, results over three speeds ($Fr = 0.28$, 0.35, and 0.41) show that the method can accurately predict the changes in resistance and free surface topology, with the two highest speeds showing bow wave breaking. For the $Fr = 0.35$ case, comparison of wave elevation results shows good agreement with the data, including the development and thickening of the bow wave sheet, sequential formation of two overturning plungers with reconnections, and the formation of two free surface scars at the reconnection sites. The computational fluid dynamics (CFD) solution shows a steep shoulder wave, similar to the experiment, but does not predict the experimentally observed weak spilling breaking shoulder wave. Although the current predictions converge to steady state, the region of unsteady free surface measured experimentally can be reasonably well predicted from the region of the simulation where the wave slope exceeds 17°. Comparisons of velocity components and axial vorticity at four cross planes show that the method can accurately predict the wake of low axial velocity and vortical cross flow associated with the breaking bow wave. In addition, the simulation is used to explain the initial development of the overturning bow wave, induced vortices and scars and to fill in the relatively sparse experimental data set by providing a global picture of the axial vortex structure near the free surface. 

Received 1 May 2006; Revised 16 October 2006; Accepted 17 October 2006

KEY WORDS: free surface; wave breaking; incompressible viscous flow; single-phase level set; surface ship

*Correspondence to: Robert V. Wilson, University of Tennessee SimCenter at Chattanooga, 701 East M.L. King Boulevard, Chattanooga, TN 37403, U.S.A.
†E-mail: Robert-Wilson@utc.edu

Contract/grant sponsor: Office of Naval Research; contract/grant number: N00014-01-1-0073

## 1. INTRODUCTION

Ship hydrodynamics presents many unique challenges due to complex geometry, environment, and operating conditions, which results in complex physics and modelling issues. Operating surface ships with high Froude (*Fr*) number, bluff geometry with appendages, and large amplitude motions and manoeuvres in waves can lead to steep, overturning, spilling, and plunging breaking waves which can produce spray, foam, and bubbles; affecting the performance of the hull and propulsion system and increasing air and water signatures. For numerical simulation of such flows, detailed resolution of complex free surface topologies is important for understanding the physics and mechanisms of air entrainment and bubble formation associated with ship wave breaking, which is one of the major sources of ship signatures. Resolving the general features of breaking waves, as performed here, should allow the development of higher fidelity models for air entrainment, bubble generation, spray generation, and free surface turbulence, as opposed to the more difficult task of modelling all of the effects of the breaking wave on a smooth free surface topology.

Until very recently (last 3–4 years), a detailed description and understanding of the breaking bow wave were not possible due to limitations mainly with numerical, but also experimental approaches. The numerical simulation of such flows is a daunting task due mainly to lack of robust-free surface models for complex topologies and lack of computational resources and numerical techniques required to resolve the wide range of scales from a few ship lengths down to the small-scale features of the overturning bow sheet and turbulent boundary layer. Although surface tracking methods, where the volume grid is dynamically fitted to the geometry and free surface, have been successfully applied to free surface flows at low to medium *Fr* [e.g. ship forward speed diffraction [1]; pitch and heave motions [2]; and DTMB 5415 roll decay [3]], it is now generally accepted that surface capturing techniques are required to manage the complex interfacial topologies associated with ships operating at high Froude number, with large amplitude motions, and in high sea states. Di Mascio *et al*. [4] presented one of the first RANS simulations of breaking waves for a practical ship geometry using a surface capturing single-phase level set method. Other such simulations include steady breaking for a wedge [5] and unsteady breaking for a surface combatant with incident waves [6]. A combined VOF/LS approach solving Euler equations was used to study flows with steep and breaking waves for a 2D NACA 0024 foil, 2D wedge, and surface combatant [7], while a two-phase level set method was used to predict pitch and heave motions for a container ship in incident waves [8]. However, comprehensive data sets containing wave elevation and near surface velocity measurements were not available to provide detailed validations for these breaking wave simulations.

Detailed wave elevation and near free surface velocity measurements are also quite difficult due to unsteadiness, free surface turbulence, spray, air entrainment, and dense measurement grids required to resolve small scales. Such measurements are also labour intensive and costly leading to relatively sparse data bases and making an overall understanding of the structure of the breaking bow wave difficult at best. With regard to spilling and plunging breaking waves, spilling breakers have been more extensively studied (for a review see [9]) and modelled (e.g. [10, 11]). Miyata and Inui [12] reviewed the structure of breaking bow waves and made near surface velocity measurements that showed a sharp transition to turbulent flow downstream of the bow wave crest, sudden energy loss and change in the velocity component normal to the wave, which allowed them to make an analogy between bow waves and oblique shock waves. Dong *et al*. [13] studied the structure of bow waves by making PIV measurements and free surface visualizations on a ship



DOI: 10.1002/fld

model for $Fr = 0.17$–$0.45$ with the focus on the initial formation of the bow wave sheet prior to the plunging event. The authors reported that the $Fr = 0.45$ case showed boundary layer separation and generation of vorticity on the model near the peak of the bow sheet. Large negative axial vorticity was also reported at the toe of the bow sheet. The vorticity produced inside the bow sheet persisted downstream at least until $x/L = 0.24$ and produced strong secondary flow of up to 20% of the ship speed. They also discovered that vorticity generated at the wave crest was transferred downstream as longitudinal vortex filaments and produced a series of small-scale free surface depressions, which contained pairs of counter-rotating vortices. Olivieri *et al*. [14] investigated wave breaking for the surface combatant and conducted a photographic study, free surface mean and root-mean-square measurements, and velocity measurements for $Fr = 0.35$. Experimental observations showed that this case contained an energetic plunging breaking bow wave with multiple free surface depressions similar to that reported by Dong *et al.* [13] and a steep spilling breaking shoulder wave.

The rapid development and integration of free surface capturing methods, local grid refinement techniques, and sufficient computational resources now allow detailed resolution of breaking bow waves and induced vortices and scars. When combined with an experimental study in a complementary fashion, these simulations can be used to further the understanding and model development for ship wave breaking. The present paper utilizes an unsteady single-phase level set method to simulate the flow over the DTMB 5415 surface combatant model in calm seas at three speeds ($Fr = 0.28$, 0.35, and 0.41), with the two highest speeds resulting in bow wave breaking. Structured overset grids are used for flexibility in grid generation and local refinement of the small-scale features of the breaking bow, shoulder, and transom waves. The current authors initially presented the method and demonstrated time-accurate free surface simulations in Carrica *et al.* [15] and applied the method to the R/V Athena research vessel at $Fr = 0.25$, 0.43, and 0.62 in Wilson *et al*. [16], which contained breaking bow and transom waves at the higher speeds. Unlike the current application, the R/V Athena study focused on high speed and did not have detailed velocity measurements available for validation. The method was also applied to the forward speed diffraction problem at $Fr = 0.28$ and 0.41 [6], which showed unsteady non-breaking and breaking bow waves, respectively.

The contributions of the current paper are (i) extension of an unsteady single-phase level set method and integration of free surface capturing and local overset refinement for resolving 3D ship breaking waves, (ii) comparison of the $Fr = 0.35$ case with detailed velocity and free surface measurements for breaking waves, and (iii) use of computational fluid dynamics (CFD) to explain the flow physics, to provide a global description of bow wave breaking and induced vortices and scars, and to fill in the relatively sparse experimental data base. In Olivieri *et al.* [14], an experimental ship wave breaking study is described in detail, where the current CFD simulations were used to help explain some of the observations in a complementary and collaborative fashion as discussed in Section 3.

## 2. CFD METHOD

The governing equations and numerical methods used in the current study are summarized in this section. The CFD method was initially presented in Carrica *et al.* [15] and readers are referred there when details are omitted. The focus here is on extensions required for the integration of the free surface capturing approach and local overset refinement for 3D ship breaking waves.



DOI: 10.1002/fld

Application of the single-phase method requires that the following two conditions must be satisfied: (i) the entire liquid–gas interface must be exposed to the ambient pressure since the continuity equation is not enforced in the air phase and (ii) the stresses on the liquid caused by the gas phase must be negligible. In addition, surface tension forces have been neglected. These simplifications allow computation of the flow in the water region only with constant properties and without pressure and velocity spurious oscillations associated with many two-phase approaches. These assumptions should be valid as long as the liquid–gas interface remains a free-boundary, as is the case for a large range of flows around free surface piercing bodies, which is the focus of the present paper. Although complex topologies can be managed with the current single-phase model, extremely small-scale features such as capillary waves, free surface turbulence, air entrainment, and bubble and drop formation due to breaking waves were not resolved here, resulting in free surface predictions that are more organized and smooth in comparison with experimental observations. Resolution of such features probably requires extremely fine spatial and temporal resolution for the free surface and flow fields, a large eddy or detached eddy simulation level of modelling, surface tension, and/or the effect of the gas motion on the liquid, which is outside the scope of the current paper.

### 2.1. Governing equations

The non-dimensional momentum and mass conservation equations for the liquid phase only are given by

$$\frac{\partial u_j}{\partial x_j} = 0 \tag{1}$$

$$\frac{\partial u_i}{\partial t} + u_j \frac{\partial u_i}{\partial x_j} = -\frac{\partial p}{\partial x_i} + \frac{\partial}{\partial x_j}\left[\frac{1}{Re_{\text{eff}}}\left(\frac{\partial u_i}{\partial x_j} + \frac{\partial u_j}{\partial x_i}\right)\right] + s_i \tag{2}$$

where $x_i$ and $u_i$ are the Cartesian co-ordinates and velocity components and $s_i$ is any volume source other than gravity. The effective Reynolds number is defined as $Re = U_0 L/\nu$, with $U_0$ a characteristic velocity (free-stream velocity) and $L$ a characteristic length (ship length). The dimensionless piezometric pressure is defined as $p = p_{\text{abs}}/\rho U_0^2 + z/Fr^2 + 2k/3$ with $p_{\text{abs}}$ the absolute pressure, and the Froude number, $Fr = U_0/\sqrt{gL}$. The Reynolds stresses are related to the mean rate of strain through an isotropic eddy viscosity $\nu_t$, which is calculated using Menter's blended $k$–$\omega$/$k$–$\varepsilon$ model without the optional shear-stress transport [17] and without wall functions. The turbulent kinetic energy $k$ and the turbulence specific dissipation rate $\omega$ are computed from transport equations.

The location of the liquid–gas interface is given by the zero contour of the level set function $\phi$, which is positive in water and negative in air. Since the free surface is a material interface (in absence of interfacial mass transfer such as evaporation or condensation), then the transport equation for the level set function is

$$\frac{\partial \phi}{\partial t} + u_j \frac{\partial \phi}{\partial x_j} = 0 \tag{3}$$

where $u_j$ is given by the velocity of the underlying flow in the water region and by an extension velocity in the air region as defined below. Since $\phi$ is a distance function, the unit normal gradient of the level set function $n_j$ points normal to the interface into the water. Approximate dynamic free



DOI: 10.1002/fld

surface boundary conditions (DFSBC) can be derived from the jump conditions on the air–water interface [18], resulting in the following conditions for velocity and pressure:

$$\left.\frac{\partial u_i}{\partial x_j} n_j\right|_{\text{int}} = 0 \tag{4}$$

$$p_{\text{int}} = \frac{z_{\text{int}}}{Fr^2} \tag{5}$$

where the subscript 'int' is used to denote quantities at the interface. Higher-order DFSBC effects (i.e. surface tension and viscous terms) are neglected in the current approximation, which is consistent with the assumptions made for the single-phase level set method above. While higher-order effects are likely to be important for small-scale features (e.g. free surface turbulence), their inclusion does not seem to be required to correctly resolve the macro-scale free surface features (e.g. free surface scars) as shown later for comparisons of simulation results to experimental measurements. Future efforts will focus on the use of two-phase level set methods with surface tension source terms included in the momentum equation, which naturally includes these higher-order effects at the water–air interface.

In order to transport the level set function, Equation (3), and also the velocities and turbulent quantities, a velocity in air is needed near the interface. Equation (4) provides a suitable velocity that at the same time satisfies the jump conditions and is solved in the entire air region to provide a velocity field in air.

### *2.2. Numerical method*

The structured, body-fitted, non-orthogonal multi-block code, CFDSHIP-IOWA is used, where the air–water interface can arbitrarily cross the multi-block and overlapping boundaries. The continuous governing equations are transformed from the physical domain in Cartesian co-ordinates $(x, y, z, t)$ into the computational domain in non-orthogonal curvilinear co-ordinates $(\xi, \eta, \zeta, \tau)$. A partial transformation is used in which only the independent variables are transformed, leaving the velocity components in the base co-ordinates. A three-level, second-order Euler backward difference is used for the time derivatives of all variables. The convective terms present in the transport equations for velocity, turbulence, and level set are all discretized using a second-order upwind method, while the viscous terms appearing for the velocity and turbulence are computed with a second-order central difference scheme. After discretization, the momentum equations are written in algebraic form as

$$A_{ijk} u_i^n + \sum_{nb} A_{nb} u_{i,nb}^n = S_{u_i} - \frac{1}{J} b_i^k \frac{\partial p^n}{\partial \xi^k} \tag{6}$$

where $A_{ijk}$ and $A_{nb}$ denote the central and neighbouring convection/diffusion coefficients of the discretized momentum equations, and $J$ and $b_i^k$ are the Jacobian and metrics of the co-ordinate transformation. The source term $S_i$ contains velocities from the previous two time steps $(n-1)$ and $(n-2)$ and the mixed derivative terms.

A pressure implicit split-operator (PISO) algorithm is used to enforce the continuity equation [19]. The mass conservation equation can be enforced by taking the discrete divergence of the discretized momentum conservation equation (6) resulting in a Poisson equation for the pressure



DOI: 10.1002/fld

of the type

$$\frac{\partial}{\partial \xi^j}\left(\frac{b_i^j b_i^k}{JA_{ijk}}\frac{\partial p}{\partial \xi^k}\right)=\frac{\partial}{\partial \xi^j}\frac{b_i^j}{A_{ijk}}\left(\sum_{nb}A_{nb}U_{i,nb}-S_i\right) \tag{7}$$

Using a second-order approximation, Equation (7) leads to a 19 point stencil. Since the contravariant pressure gradients are computed at cell faces to avoid pressure–velocity decoupling, the metrics are computed at these locations to avoid artificial mass sources. Note that Equation (7) needs to be enforced only in water, leading to a formulation with constant properties (density and viscosity of air do not appear in the equations). This is an important advantage of the single-phase level set since spurious mass sources near the interface, common in two-phase level set or VOF methods when used with curvilinear grids, are avoided.

*2.2.1. Single-phase level set.* Equation (3) is discretized as described above and solved to yield the evolution of the level set function. A key requirement of the level set function is that it remains a distance function throughout the whole computation. This is because the free surface normal is required to perform extensions and the distance is used to detect the interface location. The first neighbours to the free surface are reinitialized geometrically. The rest of the domain is reinitialized using an implicit transport of the level set function with the normals

$$n_j\frac{\partial \phi}{\partial x_j}=\text{sign}(\phi_0) \tag{8}$$

where $\phi_0$ is the non-reinitialized level set function. Since $n_j$ is a function of $\phi$, Equation (8) is nonlinear. Dirichlet boundary conditions for Equation (8) are the reinitialized close points.

Since conservation of mass and momentum are not enforced in the air region for the current single-phase method, DFSBC are used to set conditions for velocity and pressure at the interface. The zero normal gradients of the variables at the free surface are implicitly enforced by solving a transport equation for the extension Equation (4) for all points in the air region. For points in water with any neighbour in air, the pressure boundary condition, Equation (5) is used to define pressure at the air point which will implicitly set the DFSBC at the interface. Let the subscripts $p$ stand for the point in water to be computed and na for any neighbour in air. Linear interpolation leads to a condition for the pressure on the neighbour point

$$p_{\text{na}}=\frac{p_{\text{int}}}{\eta}-p_p\frac{1-\eta}{\eta} \tag{9}$$

where $\eta=\phi_p/(\phi_p-\phi_{\text{na}})$ is the distance fraction from the local point to the interface. Equation (9) is then plugged into Equation (7) for any neighbour in air to implicitly enforce the DFSBC for pressure. Note that the pressure matrix only contains points in water and the pressure in air is not necessary and does not need to be solved.

*2.2.2. Overset grids.* The CFDSHIP-IOWA flow solver utilizes overset grids, giving the code the capability to simulate flow over complex geometry and to perform local mesh refinement. For simulations without relative motion between computational blocks as considered here, use of the current level set fixed grid approach allows the intergrid interpolation coefficients to be computed once in a pre-processing step and to remain valid throughout the simulation. This is in contrast to



DOI: 10.1002/fld

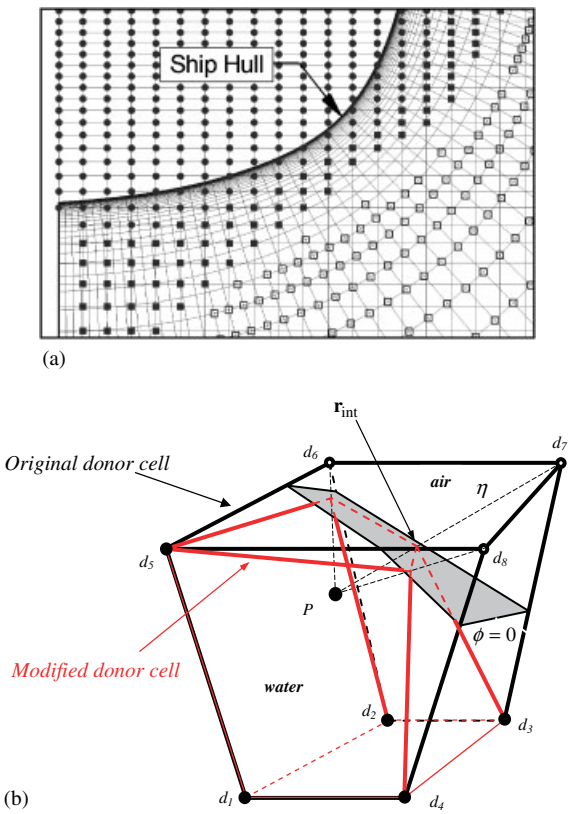


Figure 1. (a) Intergrid transfer between body-fitted boundary layer (open symbols) and Cartesian background (closed symbols) grids. Hole (circle), fringe (square), and active (no symbol) points; and (b) donor cell with grid points in air and conformation to the free surface.

the use of overset grids with a surface tracking approach, which requires the extra computational expense of recalculation of the interpolation coefficients throughout the simulation since the grid is conformed to the geometry and free surface at each time step (i.e. a dynamic overset approach). Hole cutting and connectivity information between overlapping blocks is created in a pre-processing step by Pegasus 5.1: an automated pre-processor code for overset grids, originally developed at NASA Ames Research Center for aerospace applications [20]. The double fringe layer Pegasus software option is used to allow the flow solver to retain the same higher-order five-point 1D stencil at near hole and near outer boundary points. Level-2 interpolation is also used so that minimum hole sizes are enlarged in an effort to match grid size and quality between overlapping meshes, which increases the accuracy of intergrid interpolations. Level-2 interpolation also facilitates the use of local mesh refinement, where the finer mesh is always selected as the donor mesh when two or more meshes are available. Figure 1(a) shows a detailed view of the connectivity information between body-fitted boundary layer and orthogonal background grids at the midship section.

Three basic steps are performed with this software: (i) hole cutting where points are identified as being inside or outside the solid body; (ii) identification of interpolation points that are either



DOI: 10.1002/fld

on the outer boundary of an overset block or are hole-fringe points; and (iii) identification of donor cells and associated interpolation stencils used to update interpolation points. Hole points are 'blanked out' and excluded from the solution. Two layers of fringe points are placed between active and hole points, where trilinear interpolation from other donor grids is used to define values at fringe points. After the hole cutting and connectivity information is generated for the basic grid system, the grid is decomposed into sub-blocks of roughly equal size to be used in a coarse-grain MPI-based parallel approach. The intergrid connectivity for the base grid system is post-processed to generate connectivity information for the decomposed grid, thus guaranteeing that both the base and decomposed systems have identical interpolation stencils. The grid and connectivity files for the decomposed grid are then used with other files as inputs to the flow solver.

Values at interpolation (fringe) points $f_{\mathrm{I}}$ are updated from donor values $f_{\mathrm{D}}$ after each ADI iteration sweep of the transport equations for the velocity, turbulence quantities, and level set function

$$f_{\mathrm{I}_{IB,JB,KB}} = \sum_{id=1}^{8} \alpha_{id} f_{\mathrm{D}_{id}} \tag{10}$$

where $\alpha_{id}$ denotes the interpolation coefficient and $id = 1, 8$ sweeps over the eight donor points which are associated with the interpolant at the grid point $(IB, JB, KB)$. Since valid physical equations exist for velocity, turbulence, and level set in both air and water, no special treatment is required when updating interpolation points from donor points that are either fully in air, fully in water, or around the air/water interface. However, special care must be exercised when interpolating near the interface, since a Poisson equation is solved in the water only and the pressure is not defined for grid points in the air region. The present approach removes points in air from the interpolation stencil so that only grid points in water are used along with points defined at the free surface by linear interpolation between the interpolant and the donors in air (see Figure 1(b)). For any interpolant point $P$ in water for which some of the donor points are in air, a line is defined which joins each of the donors in air with the interpolant, and the location of the free surface along each of these lines is found. At those free surface locations the pressure is known, and therefore it is a valid donor point. The location of the interface is found from linear interpolation along the line, where the weight for the interpolant is

$$\eta = \frac{\phi_d}{\phi_d - \phi_p} \tag{11}$$

and thus

$$\mathbf{r}_{\mathrm{int}} = \mathbf{r}_p \eta + \mathbf{r}_d (1 - \eta) \tag{12}$$

where $\mathbf{r} = (x, y, z)$ are the co-ordinates of any spatial point. The pressure at the new interfacial point is

$$p_{\mathrm{int}} = \frac{z_{\mathrm{int}}}{Fr^2} \tag{13}$$

The donor cell is then deformed to conform to the location of the new points in the interface, and the interpolation coefficients recomputed. This process is only necessary and performed for interpolant points in which one or more of the donor points are in air. Since the free surface location and the grids are moving in time, the cells that need to be conformed to the free surface change in time.



DOI: 10.1002/fld

Equation (10) is modified to compute the interpolant pressure when some of the donor points are in air

$$p_{I_{IB,JB,KB}} - \sum_{\text{idw}=1}^{\text{ndw}} \alpha^*_{\text{idw}} p_{\text{D}_{\text{idw}}} = \sum_{\text{ida}=1}^{8-\text{ndw}} \alpha^*_{\text{ida}} p_{\text{int}_{\text{ida}}} \tag{14}$$

where ndw and nda indicate the number of donors in water and air, respectively and $\alpha^*$ denotes the updated interpolation coefficients. The left-hand side of Equation (14) is used to set the matrix entries for the pressure Poisson equation, while the right-hand side is included in the source term since this term is known before the solution of the matrix.

### *2.3. Solution strategy*

Flow field variables are solved sequentially and a global iteration loop is used to converge nonlinearities in the coupled equations. For a typical time step, the turbulence equations are solved first, followed by the level set transport equation, which is reinitialized in two steps. The close points are reinitialized geometrically first and then all the other points are reinitialized by solving Equation (8). Since this equation is nonlinear, a few iterations are needed here to converge. Finally, the PISO algorithm is solved, which consists of predictor (implicit solution of the momentum equation) and corrector (solution of the pressure equation, with explicit update of the momentum equation) steps. The parallel implementation in CFDSHIP-IOWA is accomplished using a domain decomposition MPI-based approach. In addition to the information exchange between blocks at block-to-block interfaces, overset grid implementations need exchange of information between donor and interpolant blocks. For all equations except the pressure equation, overset interpolation information is exchanged between processors during each ADI iteration. The pressure equation is built into a sparse pressure matrix and then solved with the PETSc toolkit [21]; a parallel solver of large linear and nonlinear algebraic systems. All the interblock and overset information is built into the pressure matrix and thus no iterations are necessary to enforce the multiblock conditions.

## 3. WAVE BREAKING DATA AND SIMULATION CONDITIONS

A collaborative study between IIHR-Hydroscience and Engineering (Iowa, U.S.A.) and INSEAN (Italy) was conducted to understand 3D ship wave breaking and to obtain data for CFD code validation, resulting in detailed free surface and boundary layer measurements for the U.S. Navy surface combatant geometry [14, 22]. A photographic study was conducted over a range of speeds ($Fr = 0.28$, 0.30, 0.35, 0.325, 0.375, 0.41, and 0.45) using two barehull geosyms of the surface combatant geometry (INSEAN model 2340, $L = 5.72$ m and DTMB 5512, $L = 3.048$ m) to investigate scale effects and to identify the best speed for local flow measurements of breaking waves. It was determined that $Fr = 0.35$ represented the best compromise and was selected due to the relatively large region of bow wave breaking and steady wave pattern and the presence of a spilling breaking shoulder wave. At higher speeds, bow wave breaking is intense but unsteady and the breaking shoulder wave merges with the hull, while at lower speeds, the breaking extent and intensity are small. For $Fr = 0.35$, detailed mean wave elevations were measured in the near field using finger probes and in the far field using capacitance wire wave gauges. Wave elevation root mean square (rms) values were also measured in the near field. Three-component velocity



DOI: 10.1002/fld

measurements under the breaking wave were conducted at four axial cross-sections using a five-hole pitot probe ($x/L = 0.15$, 0.20, 0.40, and 0.50). During the measurements, the model was fixed at its experimentally measured dynamic orientation and towed at constant speed in calm water. Measurements for ship resistance and sinkage and trim are available for $Fr = 0.28$ and 0.41 from a previous collaborative effort [23], as well as wave elevation measurements for $Fr = 0.28$.

Simulations are performed at three speeds ($Fr = 0.28$, 0.35, and 0.41 with corresponding $Re = 1.26 \times 10^7$, $1.57 \times 10^7$, and $1.85 \times 10^7$) and conditions are set to match those from experiments conducted at INSEAN for the 2340 ship model in calm and deep water. The simulation sinkage and trim is fixed at the experimentally measured values for the three speeds. The focus of this paper is on the $Fr = 0.35$ case since a relatively large experimental data set exists for this condition, as summarized above. Although extensive, the experimental data set is considered sparse in comparison to information available from the CFD simulations. The $Fr = 0.28$ simulation results presented here, were originally presented in Miller *et al.* [24] in conjunction with the authors' participation in the CFD Workshop Tokyo 2005. Limited results are presented for the $Fr = 0.28$ and 0.41 simulations since the lower speed case has been studied extensively and does not contain an overturning bow wave and since local flow measurements are not available for the higher speed case.

## 4. COMPUTATIONAL GRIDS

Overlapping grids are used to allow for flexibility in grid generation and local mesh refinement for free surface waves. In general, grid points are clustered around the calm water plane in the vertical range of expected wave heights to provide adequate resolution at the free surface interface. To resolve the turbulent boundary layer at the hull surface for all cases, grid points are clustered so that the normalized near wall spacing satisfies $y^+ < 1$.

For $Fr = 0.28$ case, a three block base grid with 4.27 M total points is used, which contains an O–O topology grid from the hull surface to far field boundary with overset refinement blocks in the far field and transom stern for improved refinement of the non-breaking Kelvin wave system as shown in Figure 2. Also shown are grids for the $Fr = 0.35$ and 0.41 cases, where 6.50 and 3.84 M total grid points are used to resolve overturning bow waves, respectively. Since the $Fr = 0.35$ case is the focus of this study, the grid and flow for the $Fr = 0.41$ case is less resolved and is included here to show capability at the higher speed. A summary of grid sizes and block nomenclature for the three cases is provided in Table I. The blocking strategy for the $Fr = 0.41$ case utilizes two levels of nested grids near the expected region of the breaking bow wave. The first level of refinement is generated by selecting a portion of the background grid near the bow and by systematically doubling the number of cells in each co-ordinate direction. The second level is generated by selecting a small region of the first level refinement block and by increasing the number of cells by a factor of 1, 3, and 2 in the three co-ordinate directions, respectively. This strategy was followed because the axial resolution (the first co-ordinate direction) of the first level was deemed to be adequate, while the resolution in the cross plane direction (the second and third computational directions) was increased to better resolve the formation and development of the plunging bow breaker.

A larger grid with increased refinement is used for the $Fr = 0.35$ case in an effort to resolve some of the small-scale details of the bow and shoulder waves, which are observed experimentally. An O–O topology boundary layer block (Figure 2(c), block 1) is embedded inside a coarse Cartesian



DOI: 10.1002/fld

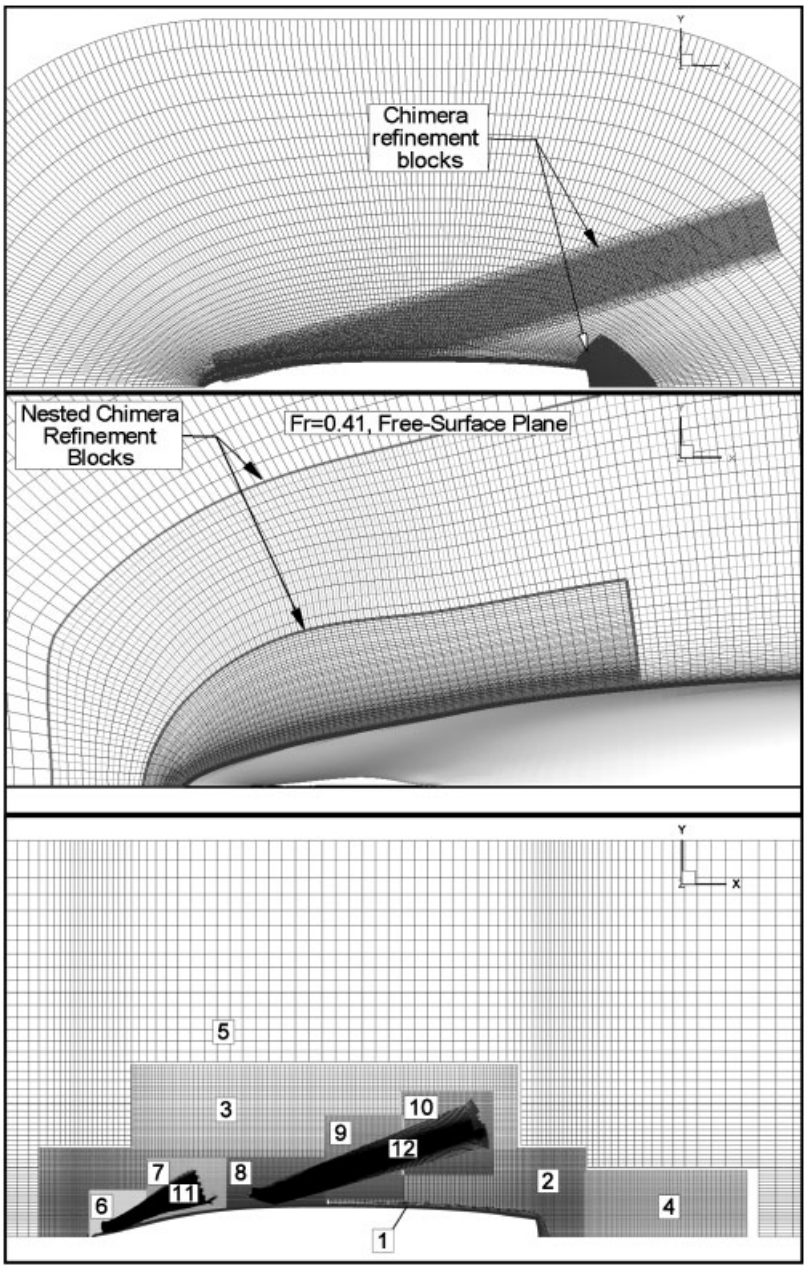


Figure 2. Computational grids at the calm water plane for $Fr = 0.28$ (top), 0.41 (middle), and 0.35 (bottom) simulations.



DOI: 10.1002/fld

Table I. Summary of grids for surface combatant in calm water simulations.

| Block no. | Block name | Grid dimension |
|---|---|---|
| $Fr = 0.28$ | | |
| 1 | Background/boundary layer | $201 \times 97 \times 119$ |
| 2 | Free surface refinement | $191 \times 69 \times 95$ |
| 3 | Transom refinement | $138 \times 71 \times 71$ |
| | | 4.27 M total |
| $Fr = 0.41$ | | |
| 1 | Background/boundary layer | $201 \times 90 \times 71$ |
| 2 | Free surface refinement, 1st level | $215 \times 53 \times 91$ |
| 3 | Free Surface refinement, 2nd level | $138 \times 91 \times 121$ |
| | | 3.84 M total |
| $Fr = 0.35$ | | |
| 1 | Boundary layer | $211 \times 51 \times 71$ |
| 2 | | $197 \times 83 \times 83$ |
| 3 | Refinement, 1st level | $103 \times 43 \times 42$ |
| 4 | | $56 \times 67 \times 42$ |
| 5 | Background | $102 \times 56 \times 43$ |
| 6 | | $64 \times 96 \times 65$ |
| 7 | | $47 \times 133 \times 65$ |
| 8 | Refinement, 2nd level | $51 \times 105 \times 57$ |
| 9 | | $41 \times 127 \times 57$ |
| 10 | | $50 \times 101 \times 57$ |
| 11 | Refinement, 3rd level (bow) | $136 \times 98 \times 99$ |
| 12 | Refinement, 3rd level (shoulder) | $137 \times 99 \times 57$ |
| | | 6.50 M total |

background block (block 5). First (blocks 2–4) and second (blocks 6–10) levels of nested overset free surface refinement blocks are added by increasing the number of cells in each co-ordinate direction of the background block (block 5) by a factor of 3 and 6, respectively. In addition, a third level of non-nested overset refinement blocks was added locally around the bow (block 11) and shoulder (block 12) waves with refinement ratio in the range, $2 < r < 4$.

## 5. STEADY STATE AND GRID CONVERGENCE

The focus of the present paper is on the development and use of modern numerical methods for simulation of complex free surface topologies around practical ship geometries, including breaking waves. This problem naturally contains a wide range of free surface scales even at the RANS modelling level: from the thickness of the overturning bow wave sheet ($\sim 10^{-4}L$) which can extend $0.15L$ into the far field, up to the scale of the Kelvin wave pattern (wavelength, $\lambda \sim 2L$ for $Fr = 0.41$). Spilling waves, possibly present in the shoulder and transom waves, could have even smaller scales and were not resolved in these computations. Also, extremely small-scale features (i.e. rough or broken free surfaces) were not resolved here. A direct numerical simulation of the ship turbulent breaking bow wave with these features is not currently viable, leading to omission or modelling at varying levels of fidelity and resolution for the foreseeable future.



DOI: 10.1002/fld

### 5.1. Verification studies

The authors have developed improvements to and advocated the use of multiple grid studies and Richardson extrapolation (RE) [25, 26], as well as procedures for code certification [27]. Assessment of numerical uncertainties for free surface ship flows at low to medium speed and with smooth topology has been successfully accomplished using this approach (e.g. [3]). However, at higher speeds ($Fr>0.3$), wave breaking typically occurs leading to complex free surface topologies and the introduction of a wide range of spatial and temporal scales, with a trend of resolving finer scale features with grid refinement (i.e. there is a strong coupling between numerical and modelling errors). A similar dilemma occurs for the assessment of numerical uncertainties in large eddy simulations, where both numerical and sub-grid scale modelling errors depend on grid resolution so that increasingly smaller scales appear with refinement. It is generally accepted that standard multiple grid studies using RE for LES flows are less than successful because the assumption that all solutions are in the asymptotic range and resolve the same scales are not met. Therefore, alternative but not yet widely accepted procedures have been proposed (e.g. [28, 29]).

Estimation of grid uncertainties using multiple solutions with systematically refined grids is not practical for the current problem, since the assumptions made for RE are not satisfied, as confirmed here using local grid refinement. Obtaining solutions on finer grids is computationally prohibitive given current resources, since the $Fr=0.35$ case uses roughly 6.50 M grid points, so that roughly 18 M fine grid points would be required using a typical grid refinement ratio of $r=\sqrt{2}$. In the absence of viable verification procedures for this problem, an alternative (albeit less desirable and conclusive) procedure was pursued here for the estimation of numerical uncertainties. For the $Fr=0.35$ case, grid convergence is assessed for resistance and free surface predictions by systematically removing the second and third levels of overset refinement and by comparing solutions on three grids with varying levels of refinement: (1) base + 3 levels (blocks 1–12, 6.50 M total grid points); (2) base + 2 levels (blocks 1–10, 4.41 M points); and (3) base + 1 level (blocks 1–5, 2.71 M points), subsequently referred to as grid systems 1, 2 and 3, respectively. Iterative convergence is assessed by examining the time history oscillations.

### 5.2. Resistance

Figure 3 shows a portion of the time history of total resistance for the three grids where the ship has advanced five ship lengths. Table II provides a summary of total, pressure, and frictional resistance coefficients along with iterative uncertainty estimates $U_I$, which are defined as half the dynamic range of the variable of interest. Iterative uncertainties for total resistance are relatively small (<0.42%) for the three grids with the highest level on grid 1, which contains three levels of refinement. Comparing results on grids 2 and 3, it can be seen that the frictional and pressure resistance changes by $\varepsilon=0.0$ and $-0.4\%$ with the addition of the second level of refinement (blocks 6–10). Since the solution change $\varepsilon<U_I$, these solution changes are smaller than the noise level so that the resistance is essentially insensitive to the addition of the second level of refinement. By comparing results from grids 1 and 2, it can be seen that slightly larger solution changes are observed with the addition of the third level of refinement and are mainly due to the drop in the pressure component (i.e. the frictional and pressure components decrease by 0.2 and 1.3%, respectively). The change in total resistance is slightly larger than the iterative uncertainty on grid 1. The resistance change with refinement can be better explained by comparing the wave profiles along the hull as shown in Figure 4. The axial pressure resistance is



DOI: 10.1002/fld

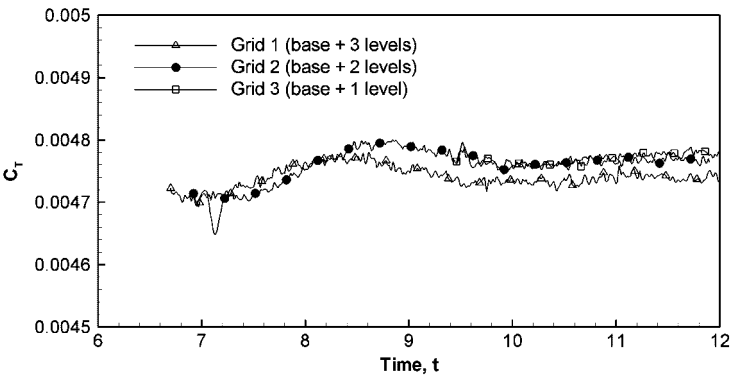


Figure 3. Convergence history for resistance coefficient $C_T$, $Fr = 0.35$.

Table II. Iterative and grid convergence for resistance predictions ($x10^3$), $Fr = 0.35$.

| Force | Grid | CFD ($\varepsilon$%) | $U_I$% |
|---|---|---|---|
| $C_T$ | 1 (base + 3 levels) | 4.739 (−0.6) | 0.42 |
| | 2 (base + 2 levels) | 4.769 (−0.2) | 0.24 |
| | 3 (base + 1 level) | 4.778 | 0.23 |
| $C_P$ | 1 (base + 3 levels) | 1.920 (−1.3) | 1.05 |
| | 2 (base + 2 levels) | 1.945 (−0.4) | 0.57 |
| | 3 (base + 1 level) | 1.952 | 0.51 |
| $C_F$ | 1 (base + 3 levels) | 2.819 (−0.2) | 0.07 |
| | 2 (base + 2 levels) | 2.824 (0.0) | 0.01 |
| | 3 (base + 1 level) | 2.824 | 0.01 |

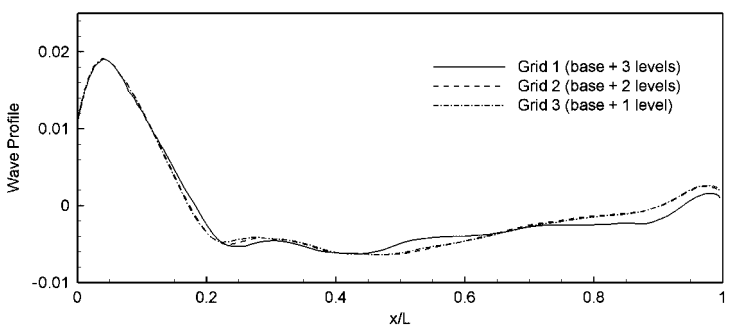


Figure 4. Effect of overset refinement on the wave profile for $Fr = 0.35$.

greatly influenced by the forward projected wetted surface area, which due to the normal vector on the hull, is determined mainly by the wave profile on the fore and after sections. Figure 4 shows that the bow wave peak is essentially the same for all three grids. As shown below, the



DOI: 10.1002/fld

Table III. Resistance predictions ($x10^3$) for surface combatant in calm water simulations.

| *Fr* | Force | CFD ($\varepsilon$%) | Data | %difference |
|---|---|---|---|---|
| | $C_T$ | 4.546 | 4.23 | 7.5 |
| 0.28 | $C_P$ | 1.538 | $C_R = 1.40$ | |
| | $C_F$ | 3.008 | ITTC 2.83 | |
| | $C_T$ | 4.739 | 4.84 | 2.1 |
| 0.35 | $C_P$ | 1.920 | $C_R = 2.04$ | |
| | $C_F$ | 2.819 | ITTC 2.80 | |
| | $C_T$ | 6.533 | 6.67 | 2.0 |
| 0.41 | $C_P$ | 3.501 | $C_R = 3.94$ | |
| | $C_F$ | 3.032 | ITTC 2.73 | |

development of the bow and shoulder waves changes with the addition of the third level of refinement for grid 1, such that the wave profile on the afterbody is reduced in comparison to that for grids 2 and 3. This reduction accounts for the drop in pressure (and thus total) resistance for grid 1.

Comparison of CFD predictions and experimental data for frictional $C_F$, pressure $C_P$, and total $C_T$ resistance is shown in Tables II and III. Good agreement is obtained for $Fr = 0.35$ and 0.41 cases with differences less than 2.1%. Agreement for the $Fr = 0.28$ case is not as close with an overprediction of 7.5% for the ship resistance, due to an overprediction in the pressure component. Comparison of the current $Fr = 0.28$ results, performed by Miller *et al.* [24] and used here, with experimental measurements (not shown) reveals that the wave profile is underpredicted on the hull afterbody and transom stern face, which leads to an overprediction for the resistance since the axial component of the normal vector points aft and the wave elevation and thus the piezometric pressure at the free surface is negative in these regions.

### *5.3. Wave contours*

Grid convergence for free surface contours is shown in Figure 5, where it can be seen that only a modest improvement in the resolution of the bow wave is obtained with the addition of the second level of refinement. However, the addition of the non-nested third level of refinement at the bow changes the structure of the breaking bow wave so that two free surface 'scars' are now observed, resulting in an improved comparison with experimental measurements, as shown below. A direct comparison can be made by examining transverse wave cuts at equally spaced cross-sections from $x/L = 0.025$ to 0.75 as shown Figure 6. The largest differences in wave elevation cuts can be seen along the breaking bow wave front $0.1 < x/L < 0.3$, where grid 1 is able to resolve multiple reconnections of the plunging bow wave, whereas grids 2 and 3 are not due to insufficient cross plane resolution. Additional differences due to grid can be seen along the shoulder wave $0.5 < x/L < 0.75$, where the free surface solution on grid 1 displays a larger and steeper shoulder wave (e.g. $x/L$, $y/L = 0.7, 0.2$) due to increased grid resolution.

Figure 7 shows a comparison of free surface contours for the surface combatant at $Fr = 0.28$, both with and without the far field and transom refinement blocks. It can be seen that the addition of the refinement blocks results in much improved resolution of the Kelvin wave pattern and



DOI: 10.1002/fld

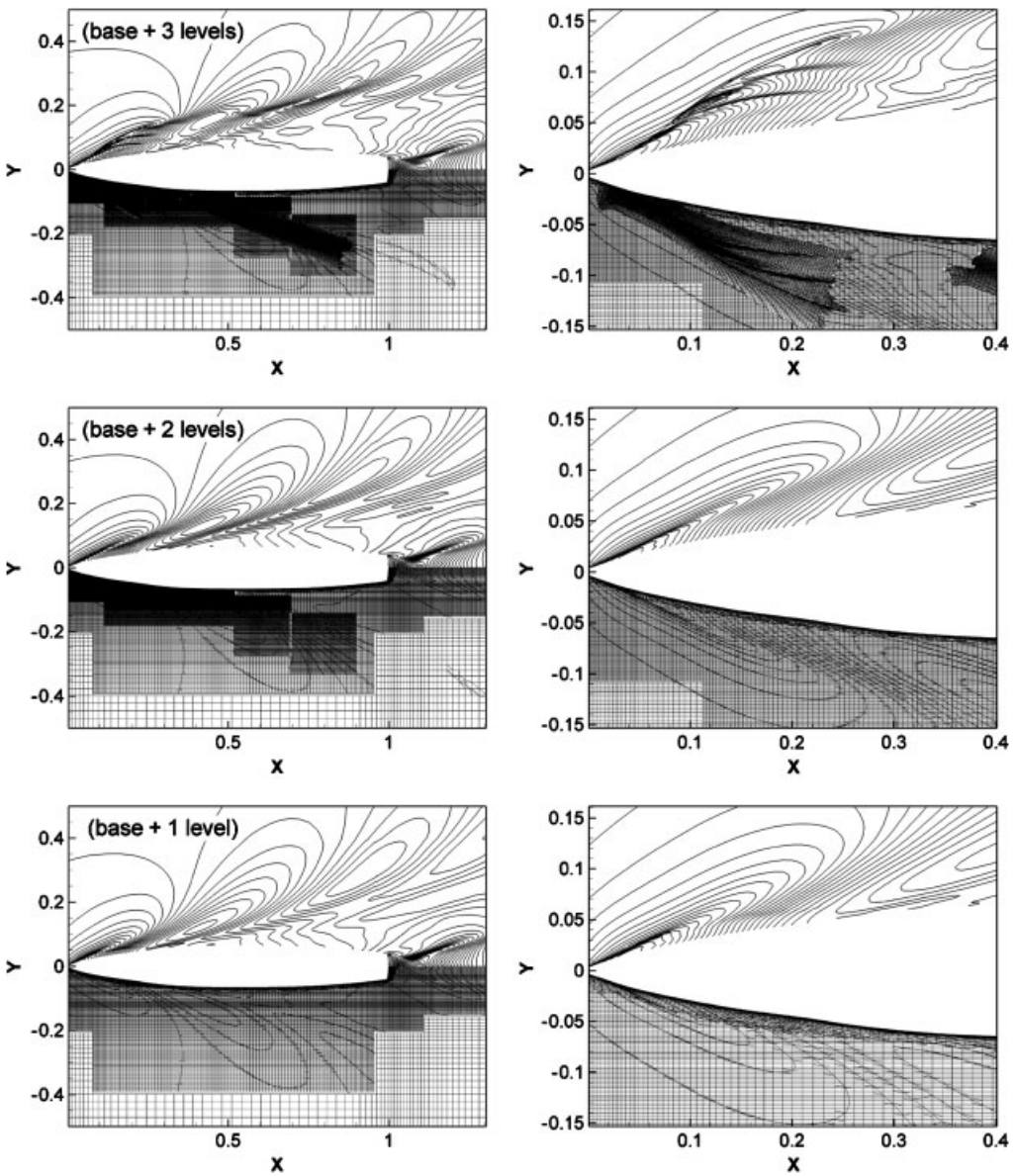


Figure 5. Effect of overset refinement on global wave contours (left) and bow wave details (right) using one (bottom), two (middle), and three (top) levels of refinement, $Fr = 0.35$.

closer agreement with experimentally measured values as shown below. Since the background grid rapidly expands from the hull surface to the far field, large transverse grid spacing leads to numerical dissipation of the far-field wave pattern for the grid system without the refinement blocks.



DOI: 10.1002/fld

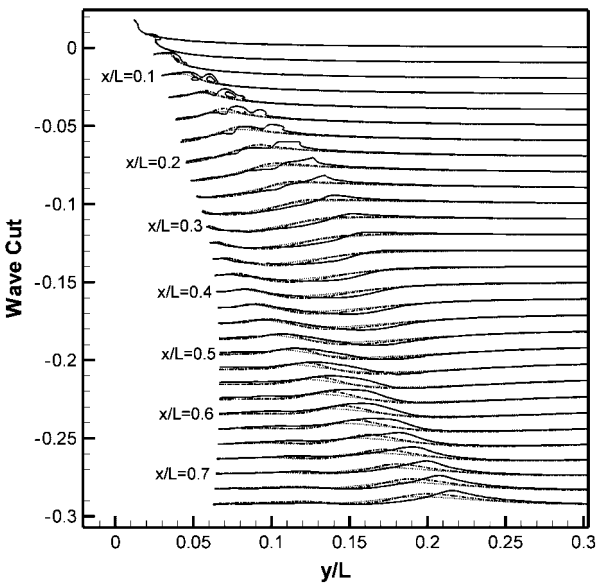


Figure 6. Effect of overset refinement on transverse wave cuts using one (dotted), two (dash-dot), and three (solid) levels of refinement, $Fr = 0.35$.

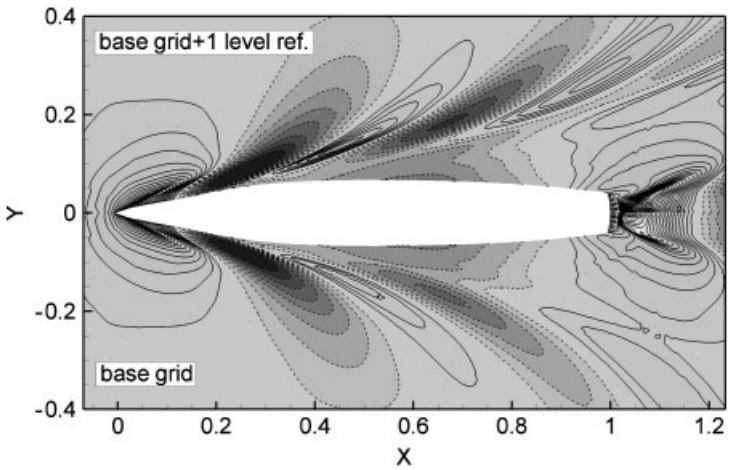


Figure 7. Wave contours from CFD solution using the base grid (bottom) and the base grid and one level of overset refinement (top), $Fr = 0.28$.

### 5.4. *Verification summary*

The assessment of grid convergence for the $Fr = 0.35$ case shows that the total resistance is both iteratively converged ($U_I < 0.42\%$) and relatively insensitive to the local grid refinement of the bow wave, with solution changes, $\varepsilon < 0.6\%$. However, the small-scale details of the bow and shoulder



DOI: 10.1002/fld

waves are very much impacted by the level of grid refinement, since the addition of the third level of overset refinement was required to correctly predict the development of the breaking bow and steep shoulder waves. The grid study results underscore the extreme resolution requirements for this problem and show that obtaining three solutions in the asymptotic range with systematic refinement is not presently practical. The difficulties in using multiple solutions for estimating grid uncertainties with these classes of problems should motivate the development of single grid uncertainty estimation methods (e.g. [30]), although their application to the 3D RANS equations using general curvilinear co-ordinates may not be straightforward or inexpensive. In subsequent sections, only solutions from grid 1 with three levels of refinement will be shown for the $Fr = 0.35$ case.

## 6. FREE SURFACE WAVE FIELD

Figure 8 shows comparisons of CFD predictions and experimental photographs of wave fields. At $Fr = 0.28$, both prediction and experiment show a relatively smooth free surface topology without large-scale plunging breaking. A closer examination of the experiment at this speed does show weak and very small-scale bow wave curling and spilling breaking of the bow and shoulder waves, which are not resolved in the simulation. As the speed is increased to $Fr = 0.35$, prediction and experiment show that the bow wave becomes steeper and overturns, forming a nearly steady plunging breaking bow wave close to the hull. In the experiment, the bow wave plunger develops some spilling and unsteadiness downstream of its crest, further out from the hull. Both the experiment and simulation develop small-scale free surface deformations on the bow wave, referred to in the literature as 'scars' and discussed later in this section. In the experiment, the shoulder wave (not shown) develops a low-energy, quasi-2D spilling wave, while the simulation predicts a very steep, but non-breaking shoulder wave. At the highest speed ($Fr = 0.41$), a strong unsteady plunging breaking bow wave is observed in the experiment with significant air entrainment, while the simulation shows a strong steady plunger. Both prediction and experiment show that the shoulder wave has merged with the hull. Figure 8 shows that extremely small-scale free surface features of breaking waves at $Fr = 0.35$ and 0.41 are not resolved in the simulations (e.g. capillary waves, free surface turbulence, air entrainment, and bubble and drop formation), leading to prediction of free surface topologies which are more coherent and smooth than those observed experimentally.

Figure 9 provides a close-up perspective view of the predicted and experimental breaking bow wave around the ship model at $Fr = 0.35$. The prediction shows the formation of a thin sheet of liquid close to the leading edge of the ship. The sheet does not separate from the hull downstream of the bow crest as observed with the plunging breaking bow waves from a research vessel at $Fr = 0.43$ and 0.62 [16], but rather thickens and develops a plunging jet which falls and reconnects with the free surface below, forming a pocket of air which remains exposed to ambient pressure (i.e. a pressurized bubble is not formed). After reconnection, a second overturning plunger is formed followed by a second reconnection. Two localized small-scale free-surface scars are formed in between the pockets of air, which originate from the point of reconnection and persist into the first trough downstream of the breaking bow wave, as labelled in Figure 9. Two scars are also observed in the experimental photograph.

A comparison of global wave patterns and bow details from predictions and EFD measurements is provided in Figure 10 for the $Fr = 0.35$ case. The predicted bow, trough, and shoulder wave structures are in very good agreement with the experimental measurements. The effects of the breaking bow plunger can clearly be seen on the wave pattern, which shows deviations from a



DOI: 10.1002/fld

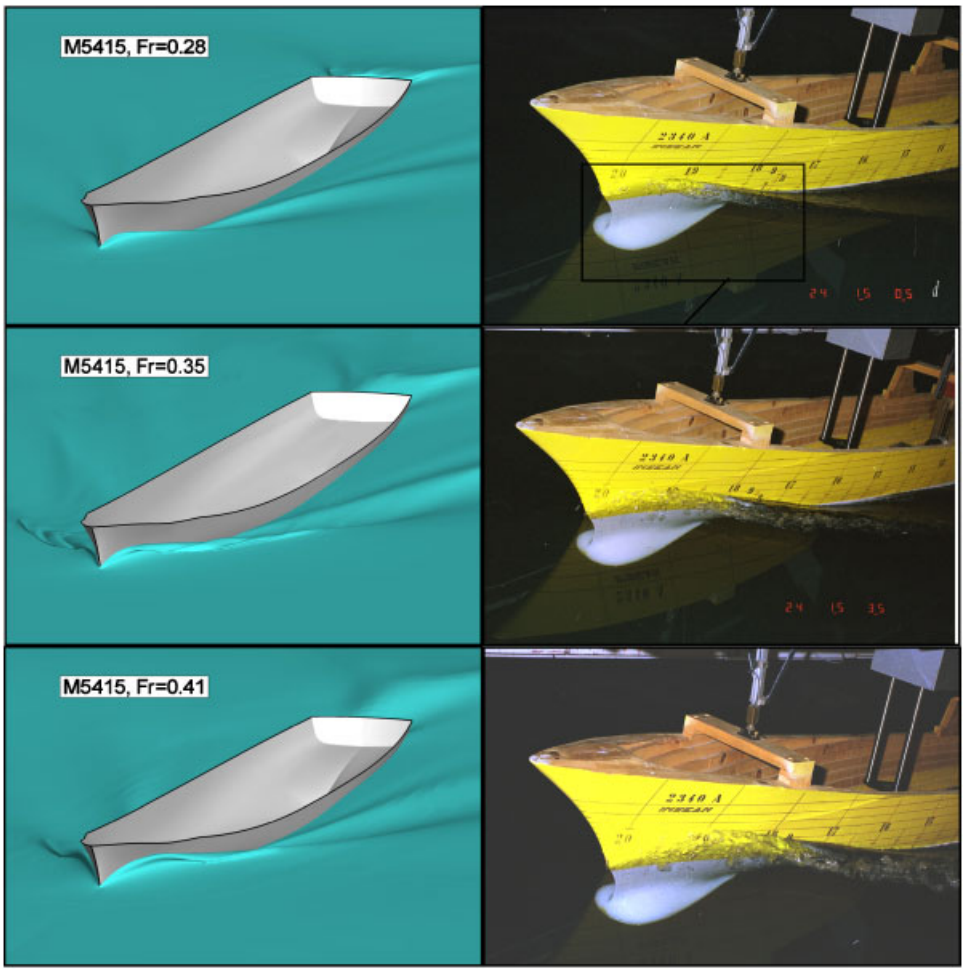


Figure 8. Comparison of CFD solutions (left) and experimental photographs (right) for the three speeds.

classical Kelvin pattern. The CFD solution displays three bow wave contour maximums separated by two scars as discussed above and labelled in Figure 10. The solution also shows evidence of a weak third scar at the tail end of the breaking wave front. The CFD tends to overpredict the second and third maximums, while the data only show a weak third maximum. The predicted plunger formation, reconnection, and rebound is more coherent than that for the experimental flow which shows a rough and broken free surface (see Figure 9), leading to an overprediction in wave elevation maximums. Also in agreement with the data, the CFD prediction shows a more steep and sharp shoulder wave, which is also atypical of classical Kelvin patterns.

Experimental measurements of the rms of the fluctuating wave height $H_{\mathrm{rms}}$ are shown at the bottom of Figure 11, where the largest values occur in the breaking bow wave region, particularly along the two free surface scars with levels as high as 10% of the maximum wave height. Higher rms levels are also present along the crest of the spilling shoulder wave with levels of roughly 5% of the



DOI: 10.1002/fld

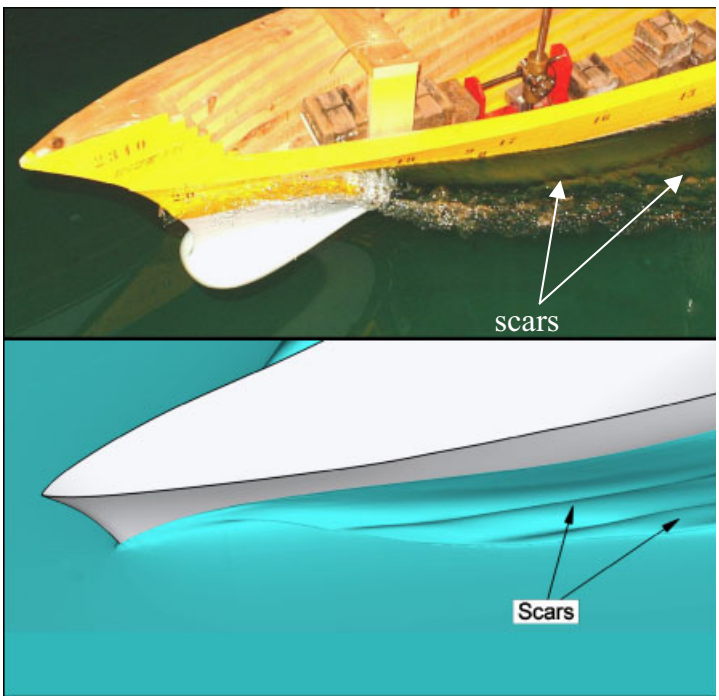


Figure 9. Bow wave details for CFD solution (bottom) and an experimental photograph (top), $Fr = 0.35$.

maximum wave height. High rms levels measured experimentally are associated with turbulent and broken free surface topologies, which were not captured in the steady CFD solution. In Duncan [31], a local wave steepness criterion of $\theta = 17.1^\circ$ was proposed to predict the inception of 2D spilling breaking. Following Olivieri *et al*. [14], which showed a correlation between the experimentally measured wave slope and rms wave elevation, an attempt is made to correlate this criterion with wave breaking. The wave slope from the CFD solution is compared with wave elevation rms contours in Figure 11, where the $H_{\text{rms}} = 0.0005$ contour level from the measurements is included to indicate the extent of experimental unsteady wave breaking. The forward $H_{\text{rms}} = 0.0005$ contour denotes the area of unsteady bow wave breaking, while the downstream contour indicates that for the crest of the spilling shoulder wave. The figure shows that the wave slope from the CFD solution exceeds the 17° criterion on the forward and rear face of the shoulder wave for $x/L > 0.45$. Large wave slope is also predicted where the shoulder wave meets the hull near $x/L = 0.3$ and within the breaking plunging bow wave, which correlates with the regions of high levels of wave elevation rms. Also of note is the correlation between the two striations of measured rms contours and predicted large wave steepness at the location of the previously discussed free surface scars. The angle criterion is also exceeded at the edges of the Kelvin wave envelope of the transom wave system (not shown here), where spilling breaking is observed experimentally. It appears that the Duncan criterion can be used to predict regions of free surface turbulence from RANS predictions, even though the simulation yields a steady wave pattern.

A more quantitative comparison of the wave field is provided in Figure 12, where transverse wave cuts from $x/L = 0.05$ to 0.7 are directly compared. The comparison shows that the largest



DOI: 10.1002/fld

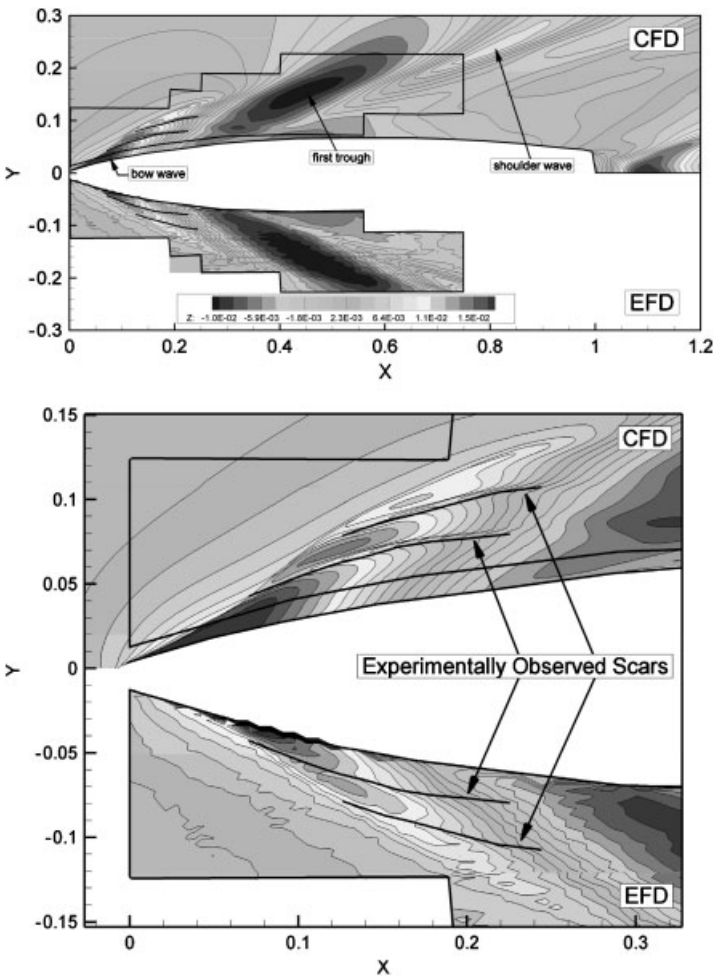


Figure 10. Comparison of CFD solution and measurements for global wave contours (top) and bow wave details (bottom), $Fr = 0.35$.

differences for the bow wave are at transverse locations corresponding to local maximums, where the CFD shows the largest overprediction (12% of the maximum elevation) at $x/L = 0.1$, where the second plunger is reconnecting with the free surface below. The CFD solution predicts a minimum wave value of $-0.0110$ for the first trough compared to $-0.0117$ from experiments, giving a difference of only 3.5% of the maximum wave elevation. By examining Figure 10 and wave cuts from $x/L = 0.4$–$0.5$ in Figure 12, it can be seen that the size of the trough is smaller and its location is shifted slightly upstream in comparison to the data. The height of the shoulder wave crest is also in very close agreement with the data (e.g. at the last experimental cross-section of $x/L = 0.74$, the solution shows a maximum shoulder elevation of 0.0688 compared with a data value of 0.0696, giving a 4% difference), with the CFD solution showing underprediction on either side of the shoulder wave crest. The experimental wave also shows steeper slopes in the



DOI: 10.1002/fld

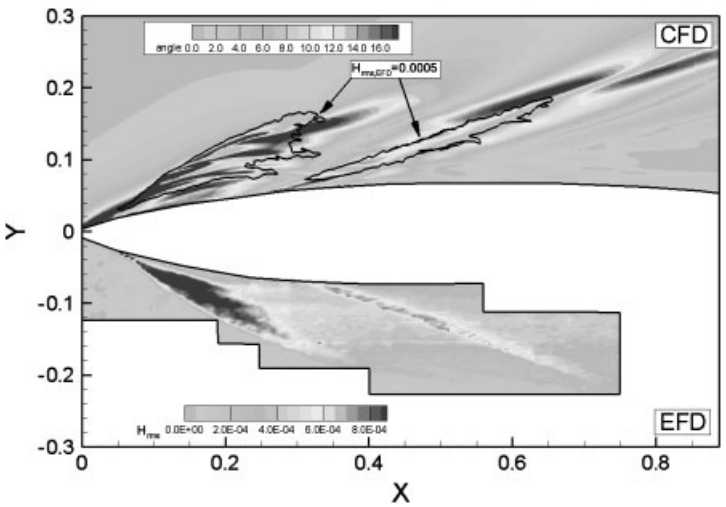


Figure 11. Comparison of wave slope from CFD prediction in degrees (top) and wave elevation RMS from measurements (bottom), $Fr = 0.35$.

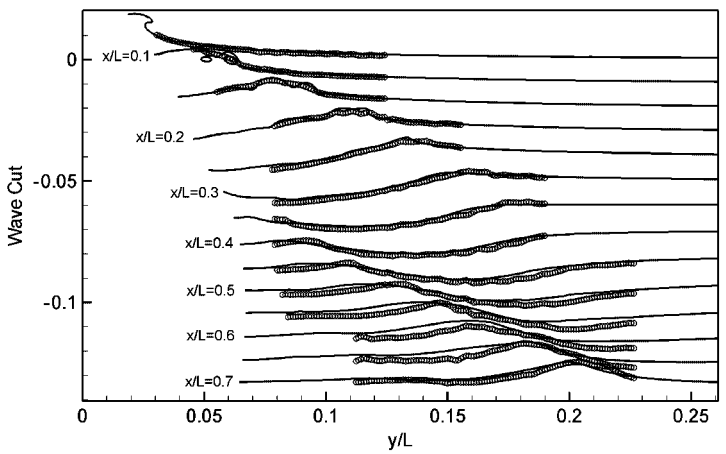


Figure 12. Comparison of CFD solution (lines) and measurements (symbols) for transverse wave cuts, $Fr = 0.35$.

transverse direction. Recall that the experimental observation shows an unsteady spilling breaking wave, while the CFD predicts a steep, but non-breaking shoulder wave, which may explain the differences discussed above. Additional grid refinement and/or a two-fluid free surface model may be required to simulate the low-energy, quasi-2D spilling wave.

Figure 13 shows a comparison of free surface contours with measurements at $Fr = 0.28$. It can be seen that the addition of the refinement blocks results in a much improved resolution of the Kelvin wave pattern and closer agreement with experimentally measured values. Figure 13 also shows the CFD wave elevation contours for $Fr = 0.41$, where the height and wavelength of the



DOI: 10.1002/fld

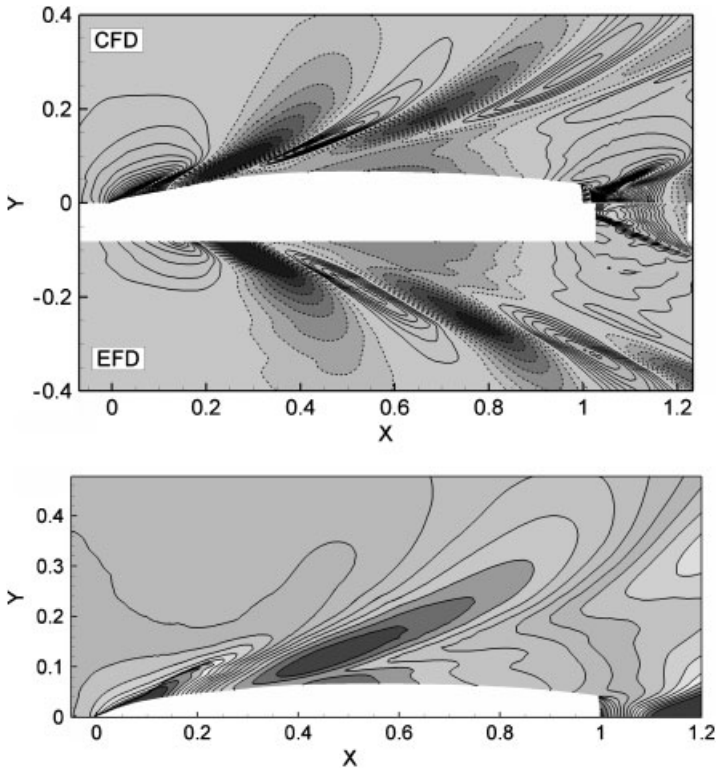


Figure 13. Comparison of wave contour CFD solution and measurements for $Fr = 0.28$ (top) and CFD solution for $Fr = 0.41$ (bottom).

breaking bow wave are increased as expected. Unfortunately, wave elevation measurements are not available for comparison at this ship speed.

## 7. BOUNDARY LAYER AND FREE SURFACE VORTICES

The effects of the breaking wave field on the turbulent boundary layer and its generation of vorticity at the free surface are discussed here. Comparisons with boundary layer measurements are made and then the CFD solution is used to fill in the sparse experimental data set and to explain the formation and evolution of the overturning bow wave.

### *7.1. Data comparison*

Comparisons of predicted and measured velocity components and axial vorticity are shown in the four data planes $x/L = 0.15$, 0.2, 0.4, and 0.5 in Figures 14–17, respectively. To aid in the comparisons, an outline of the measurement region is included with the predicted contours and vortices V1–V8 (discussed later and identified in Figure 18) are labelled in the figures along with their rotational orientation (CW: clockwise and CCW: counter-clockwise). Also of note is



DOI: 10.1002/fld

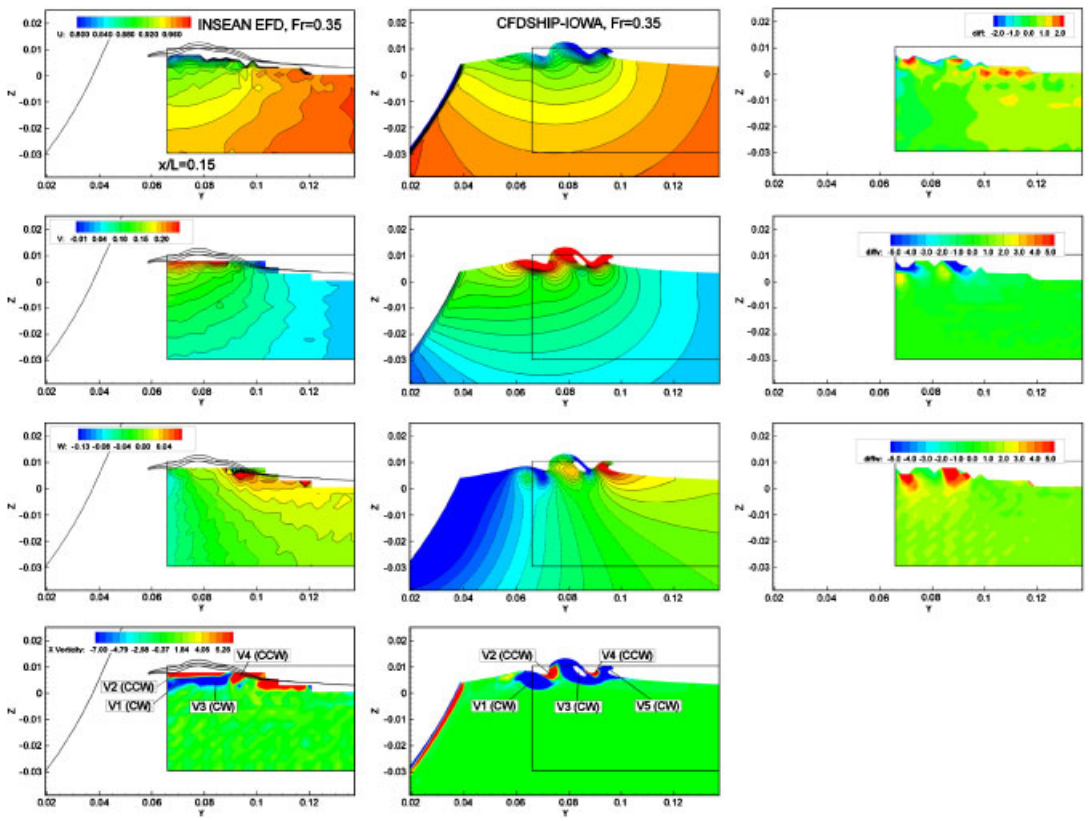


Figure 14. Velocity and axial vorticity measurements (first column) and predictions (second column) and comparison difference $100 \cdot (D - S)/U_0$ (third column): $x/L = 0.15$, $Fr = 0.35$.

the magnified range of axial velocity contours required to show the boundary layer structure (i.e. 19, 16, 8, and 10% of the freestream velocity $U_0$ for the four cross-sections) and the fact that the velocity measurements do not extend all the way to the free surface, as can be seen by the gap in between the contours and the lines of measured free surface elevation in the figures. During the initial comparisons of axial velocity contours, a small systematic difference between predictions and measurements was observed for the last two data planes ($x/L = 0.4$ and 0.5), where the predictions were uniformly higher than that of the data for 1.9%. It is speculated that there could be a small systematic error, possibly due to calibration of the probe with respect to the freestream velocity which is used to non-dimensionalize the axial velocity measurements. Taking into consideration the systematic difference and the small magnified ranges, a constant value of $-1.9\%U_0$ was added to the axial velocity predictions at both $x/L = 0.4$ and 0.5. Although the uncertainty in the axial velocity prediction $U_{SN}$ was not estimated, the 1.9% correction is very likely to be smaller than the combined uncertainty $U_V = \sqrt{U_D^2 + U_{SN}^2}$ from the simulation $U_{SN}$ and the data ($U_D = 1.3\%U_0$), i.e. the correction is within the noise level of the data and simulation.

The first cross-section ($x/L = 0.15$) is positioned within the breaking bow wave, where two plunger and reconnection events have taken place, generating a 'wake' of low-speed axial velocity



DOI: 10.1002/fld

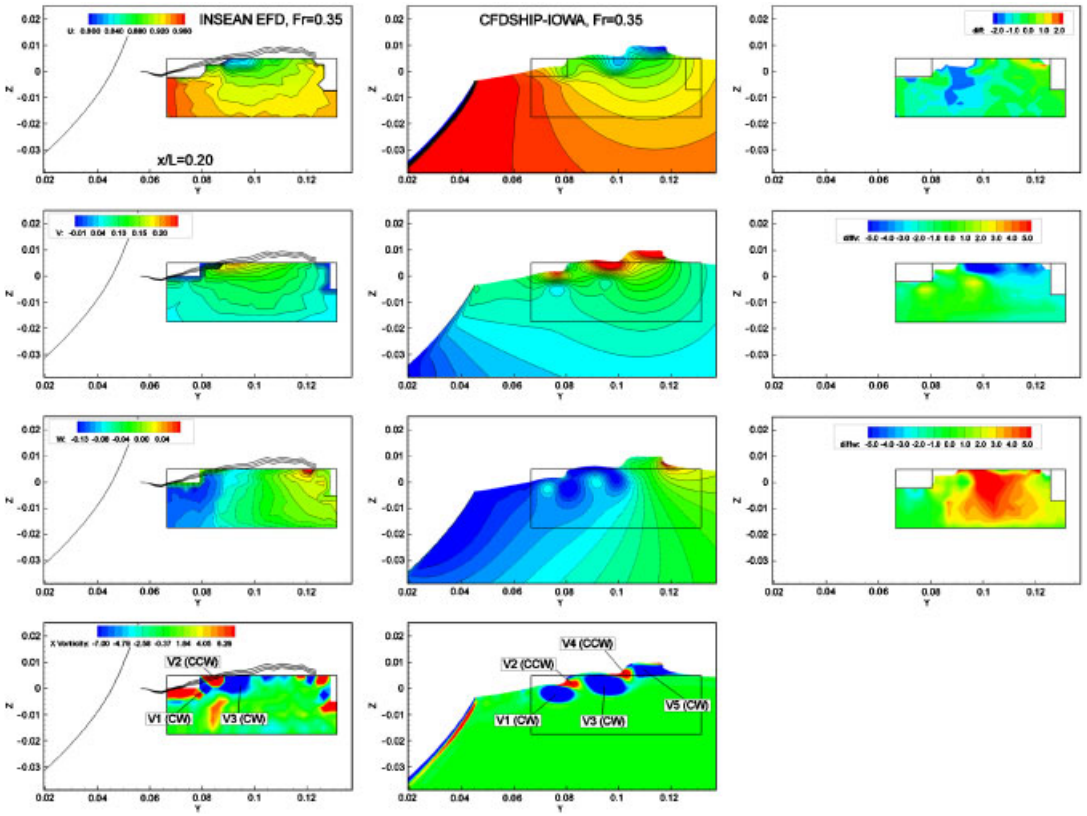


Figure 15. Velocity and axial vorticity measurements (first column) and predictions (second column) and comparison difference $100 \cdot (D - S)/U_0$ (third column): $x/L = 0.20$, $Fr = 0.35$.

with large gradients at the free surface and vortices V1–V5 as shown in Figure 14. At this cross-section, the pocket of air associated with the first reconnection has closed, while the one from the second is clearly visible. The level of agreement with the data for the axial velocity contour magnitude and shape at this cross-section is excellent. Two regions of negative vorticity can be identified in the data and predictions (labelled V1 and V3 in Figure 14), and it appears that V1 is only partially within the data region at this cross-section. In addition, two regions of positive vorticity are also tentatively identified and labelled as V2 and V4 for the data, since they are very close to the free surface and their identity is less certain. It is difficult to compare the flow and to identify vortices in the data very close to the free surface, since velocity measurements are not made there, which may be why not all of the vortices identified in the CFD solution can be seen in the data of Figure 14. Comparisons of the cross flow $V$ and $W$ contours show the largest differences from the data near the first and second plunger reconnections, with the CFD solution showing reduced transverse velocity $V$ below V1 and V3 and higher (lower) vertical velocity $W$ to the left (right) of V1 and V3. The induced cross flow velocity is consistent with the rotation of the two vortices V1 and V3. The larger induced cross flow in the prediction is probably due to the fact that the plunger formations and reconnections are more smooth and coherent in



DOI: 10.1002/fld

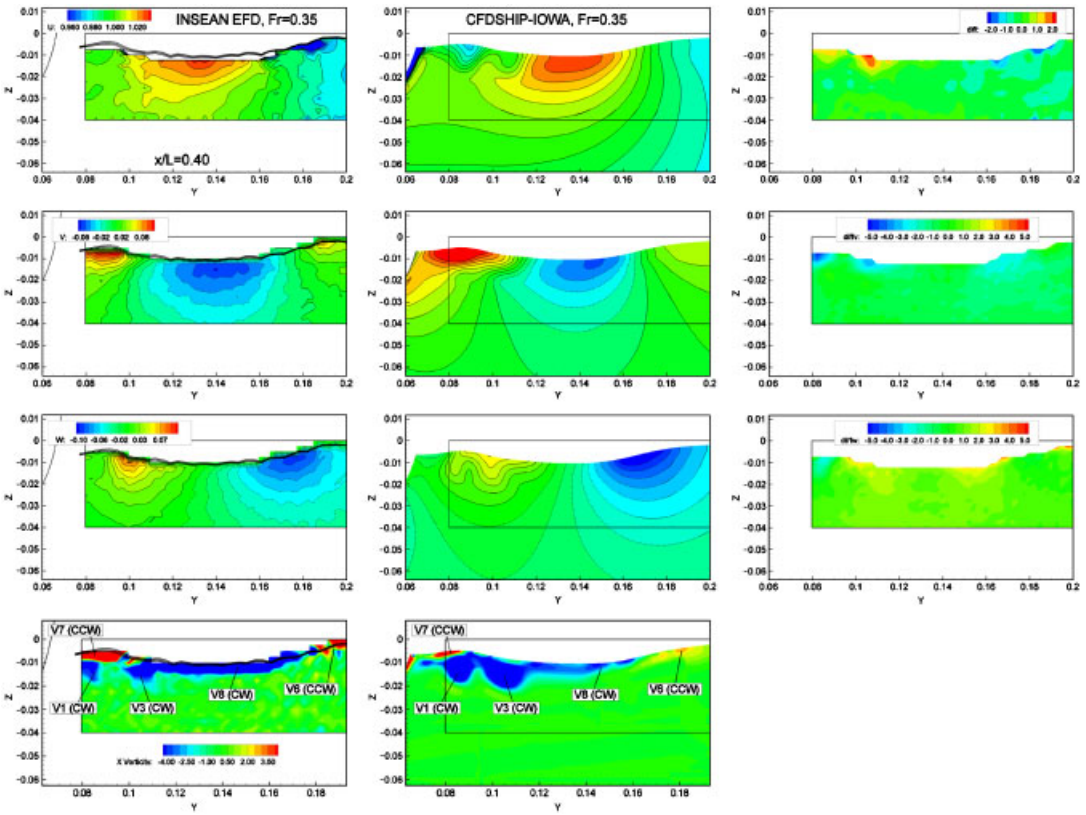


Figure 16. Velocity and axial vorticity measurements (first column) and predictions (second column) and comparison difference $100 \cdot (D - S)/U_0$ (third column): $x/L = 0.40$, $Fr = 0.35$.

comparison to the experiment, yielding overprediction for the free surface, and thus the cross flow velocities.

The second cross-section ($x/L = 0.2$) is positioned at the tail of the breaking bow wave, where the three free surface pockets that formed upstream are now closed, although the wake of axial velocity and the vortices V1–V5 associated with their formation are evident, as shown in Figure 15. The predicted features of the axial velocity wake are in close agreement with the data (i.e. the hook-shaped contours at $y, z = 0.08, -0.01$ and large vertical gradients at the free surface due to the rotational orientation of V1 and V3). Reasonably good agreement between the predicted and measured cross flow can be seen at this cross-section, although the CFD solution again tends to overpredict the cross flow induced by the vortices V1–V5 close to the free surface.

Further downstream at $x/L = 0.4$ and 0.5 (positioned just upstream of the first trough and shoulder wave, respectively), Figures 16 and 17 show that the main feature of the axial velocity is the presence of a maximum at the free surface and under the first trough region due to the acceleration of $U$ from the favourable free surface pressure gradient at this location. V1 and V3 can clearly be seen in both the prediction and data, with close agreement in both location and magnitude. Also shown in these two cross-sections are the weaker and more diffused vortices



DOI: 10.1002/fld

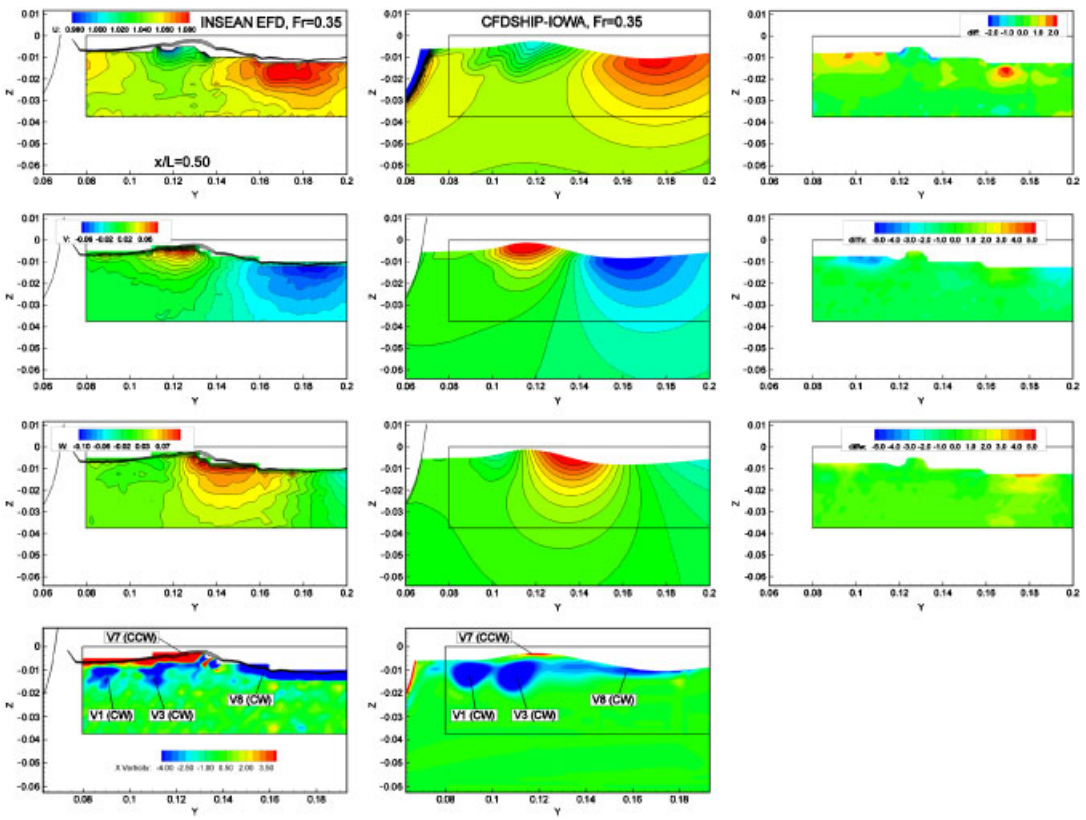


Figure 17. Velocity and axial vorticity measurements (first column) and predictions (second column) and comparison difference $100 \cdot (D - S)/U_0$ (third column): $x/L = 0.50$, $Fr = 0.35$.

V6–V8. In both the prediction and the data, the rotational orientation of V1 and V3 gives rise to distortions in the axial velocity contours at $x/L = 0.4$, although that for the CFD is more pronounced. Comparisons of the cross flow at the last two cross-sections again show very good agreement with differences in contour maximums and minimums of less than 4% $U_0$.

Comparisons of velocity and axial vorticity predictions with data have been performed to validate the CFD solution at two planes crossing the later stages of the breaking bow wave and two planes downstream of the beginning of the first trough and shoulder wave. With the close agreement between predictions and measurements, the CFD solution is now used to provide a global picture of the vorticity structure, to explain the initial development of the breaking bow wave, and to fill in the relatively sparse experimental data set.

### 7.2. *Vorticity structure*

Axial vorticity contours from the $Fr = 0.35$ simulation are shown in Figure 18 at equally spaced cross-sections ($\Delta x = 0.0172$), where eight free surface vortices are identified and labelled as V1–V8 using either red (positive vorticity) or black (negative vorticity) lines. Vortices V1–V6 are associated with the overturning bow wave, while V7 and V8 are weaker and associated with



DOI: 10.1002/fld

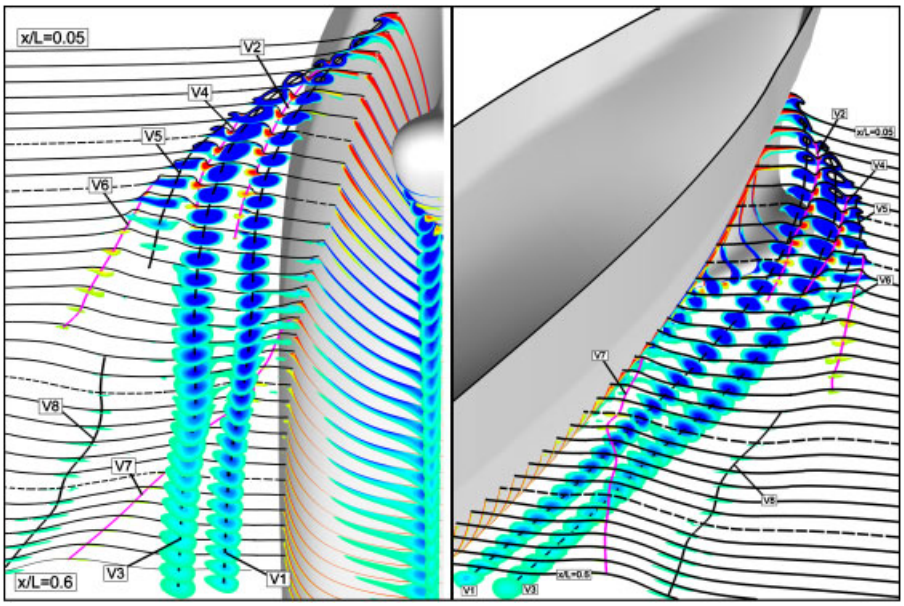


Figure 18. Axial vorticity contour slices and vortex nomenclature from CFD solution with under free surface (left) and above free surface (right) views, $Fr = 0.35$. Dashed lines indicate data planes, $x/L = 0.15$, 0.2, 0.4, and 0.5.

the shoulder wave and first trough, respectively. The location of the vortex cores was found by tracing concentrations of axial vorticity near the free surface from $0.05 < x/L < 0.6$. V1 and V3 with negative vorticity are formed due to the reconnection of the first and second plunging tips, respectively, while V2 and V4 with positive vorticity are formed in between V1/V3 and V3/V5, respectively, and are associated with the two free surface scars. It appears that a third, much weaker, reconnection/scar event is present outboard of the first two, which gives rise to V5 and V6. V1 and V3 persist past the midship section and interact with the shoulder wave and trough vortices V7 and V8, which are an order of magnitude smaller than V1 and V3. A sheet of axial vorticity can also be seen on the hull surface, which is associated with the tilting and stretching of vorticity within the turbulent boundary layer as the flow is turned by the bow and sonar dome. Positive vorticity within the sheet is transported into the first plunging tip at the free surface (see $x/L = 0.05$ cross-section), while negative vorticity within the sheet around the sonar dome is responsible for the shedding of vortices into the wake, which can clearly be seen near the ship centreplane in Figure 18.

The structure of the free surface vortices for the $Fr = 0.28$ and 0.41 simulations is shown in Figure 19 for the region $0.05 < x/L < 0.6$. Axial vorticity slices are shown together with wave elevation contours and concentrations of axial vorticity are denoted with lines as in Figure 18. The figure shows that relatively low levels of axial vorticity and weak free surface vortices are associated with the non-breaking $Fr = 0.28$ case. As shown in the figure, positive (negative) vorticity is associated with the wave crests (troughs), respectively. Recall that the $Fr = 0.41$ case displays a breaking bow wave with the formation of one plunging tip, which generates a strong vortex along the breaking bow wave front and extends downstream to the first trough, as indicated in Figure 19.



DOI: 10.1002/fld

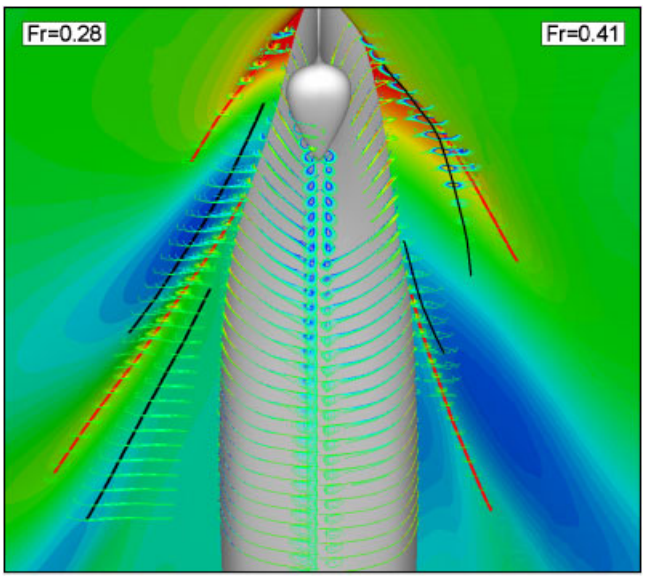


Figure 19. Axial vorticity slices and free surface contours for $Fr = 0.28$ and 0.41 simulations.

### 7.3. *Initial stages of bow wave breaking*

The initial evolution of the bow wave from the $Fr = 0.35$ simulation is now explained by examining axial vorticity with cross flow vectors, cross flow magnitude, and turbulent kinetic energy at four cross-sectional planes ($x/L = 0.02$, 0.062, 0.075, and 0.089) through the breaking bow wave as shown in Figure 20. At the first cross-section ($x/L = 0.02$), which is upstream of the bow wave crest and subsequent breaking, a steep bow wave has begun to form due to the turning of the flow at the leading edge of the bow. Also shown is the large turbulent kinetic energy $k$ and the sheet of positive vorticity contained within the turbulent boundary layer, as well as negative vorticity at the base of the forming bow wave due to higher transverse velocity at the steepest portion of the bow wave. The second cross-section ($x/L = 0.062$) is located at the bow wave crest, where the first plunger has already formed due to the larger transverse velocity at the crest and is falling towards the free surface below. As described for the breaking bow wave associated with the Athena research vessel at $Fr = 0.43$ in Wilson *et al.* [16], this results in large differences in the cross plane velocity components in the plunger tip and the free surface below as shown by contours of cross flow magnitude in Figure 20 at $x/L = 0.062$. Note that positive axial vorticity and turbulent kinetic energy are transported from within the turbulent boundary layer towards the plunging tip. At the third cross-section $x/L = 0.075$, the tip has reconnected with the free surface resulting in the generation of a counter-rotating vortex pair at the newly formed toe region due to the large jump in velocity components across the reconnection. This vortex pair has a rotational orientation that pumps fluid outboard at the toe and is responsible for the formation of the second plunger visible at $x/L = 0.089$ and the resulting scar that appears between the two pockets. The vortex pair results in a large acceleration of the cross flow in a short distance across the reconnection region, which creates a turbulent kinetic energy source and the generation of large $k$, which is transported downstream for several ship lengths. Regions of negative axial vorticity can



DOI: 10.1002/fld

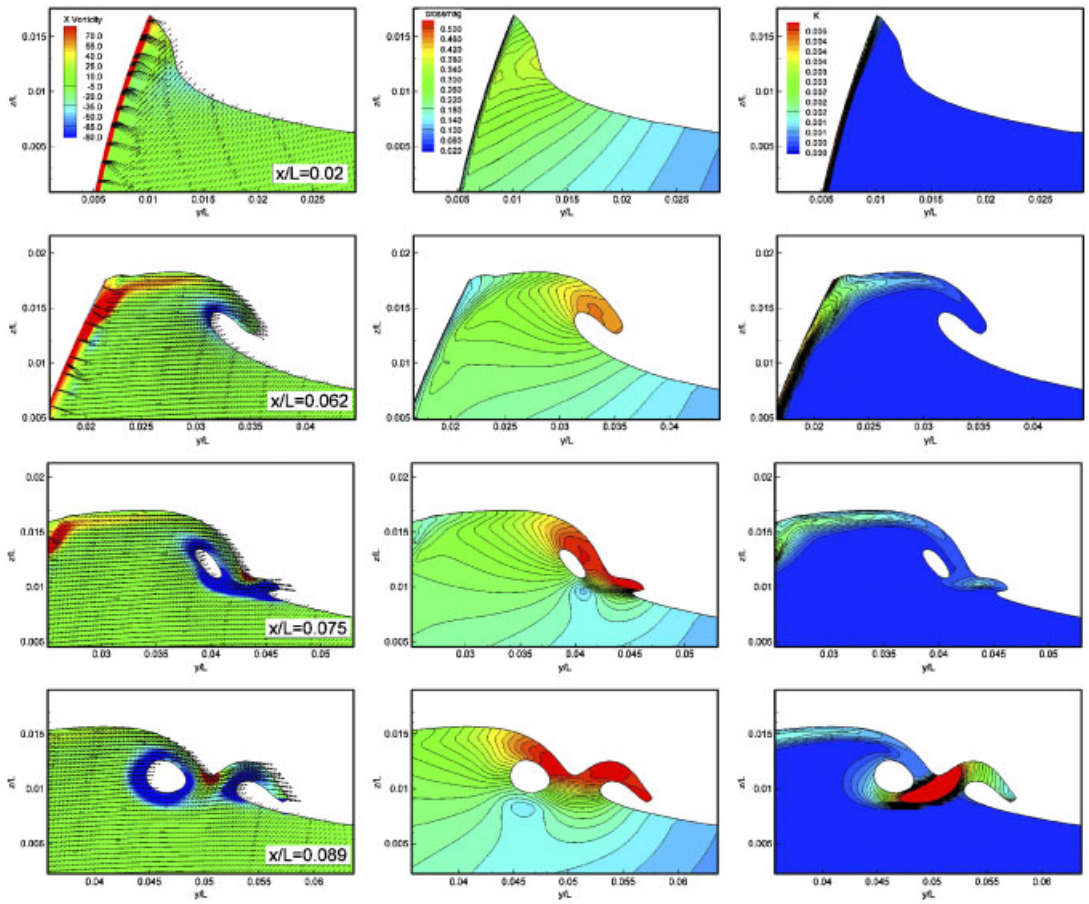


Figure 20. Initial bow wave development at four cross-sectional planes: axial velocity with cross flow vectors (first column), cross flow velocity magnitude (second column), and turbulent kinetic energy (third column) from CFD solution, $Fr = 0.35$.

be seen at the top and bottom of the elongated pocket due to the flow being turned and eventually merge to form a closed region of vorticity around the entire circumference. The last cross-section ($x/L = 0.089$) shows the development of the first free surface scar in between the closed first pocket and newly formed second plunger. Recall that the bow wave development downstream of the second plunger reconnection was previously discussed in the data comparison section (see Figures 14 and 15).

## 8. SUMMARY AND CONCLUSIONS

An unsteady RANS single-phase level set method was extended and integrated with local overset grid refinement to resolve small-scale features of 3D ship breaking waves. For the current



DOI: 10.1002/fld

model, conservation of mass and momentum is enforced in the water region only and DFS-BCs are used to set conditions at the interface. Capability for local grid refinement is provided through the use of an overset grid approach, where static hole cutting and generation of intergrid connectivity information are accomplished in a pre-processing step using a popular overset grid processing software. The unsteady RANS single-phase model tends to predict a breaking bow wave which is more coherent, steady, and smooth than that from experiment. Resolution of extremely small-scale unsteady free surfaces will probably require increased spatial and temporal resolution, large eddy or detached eddy simulation modelling, surface tension, and/or the effect of the gas motion on the liquid, which is outside the scope of the current paper.

Steady-state iterative uncertainties were estimated by examining resistance time histories, while grid uncertainties for resistance and wave elevations were addressed by systematically removing the second and third levels of overset refinement and comparing solutions on the resulting three grids. Results at medium speed ($Fr = 0.28$) show a smooth free surface topology with a classical Kelvin wave pattern in agreement with data, while those at two higher speeds ($Fr = 0.35$ and 0.41) show bow wave breaking. Comparisons for the $Fr = 0.35$ case show that the bow wave structure is well predicted, including the development and thickening of the bow wave sheet, sequential formation of two overturning plungers and reconnections, and the formation of two free surface scars at the reconnection sites. Excellent agreement with the data was obtained for the location and extent of the two scars. The first trough wave minimum and shoulder wave crest are well predicted with differences less than 3%. The CFD solution shows a steep shoulder wave, similar to experiment, but does not show the experimentally observed weak spilling breaking shoulder wave. Although the current predictions converge to steady state, an important result from the current study is that the region of unsteady free surface measured experimentally for the bow and shoulder waves can be reasonably well predicted from the region of the simulation where the wave slope exceeds 17°. This result should aid in the development of higher fidelity models for air entrainment, bubble and spray formation, and free surface turbulence due to breaking waves.

Comparison of velocity components and axial vorticity at four cross planes shows that the method can accurately predict the wake of low-speed axial velocity and vortical cross flow associated with the breaking bow wave and the acceleration and deceleration of the flow due to the first trough and shoulder waves. The solution is used to fill in the relatively sparse experimental data set by providing a global picture of the axial vortex structure under the free surface, which would not have been possible without the use of the CFD. The initial development of the overturning bow wave was also explained using the CFD solution, where it was shown that the initial plunger was created due to the formation and subsequent thickening of the bow wave sheet. The reconnection of the first plunger is associated with large cross flow differences between the plunger tip and free surface below, generation of large turbulent kinetic energy, the formation of a free surface scar, and axial vorticity with a rotational orientation that results in the formation of a second plunger and reconnection.

The current work shows that the collaborative use of both experimental and computation studies and the recent and rapid developments for free surface capturing methods, local grid refinement, and available computational resources now allow for a detailed resolution and investigation of 3D ship breaking bow waves and a further understanding of such flows. Capabilities for dynamic overset grids required for prediction of large amplitude ship motions were recently added to the CFD method and will be reported elsewhere [32].



DOI: 10.1002/fld

ACKNOWLEDGEMENTS

This research was sponsored by Office of Naval Research grant N00014-01-1-0073 under the administration of Dr Patrick Purtell. The authors would like to acknowledge the DoD High Performance Computing Modernization Office. Simulations were performed at the Army Research Lab Major Shared Resource Center using both the SGI Origin 2000 and 3000 machines. The authors would like to thank Mr Ronald Miller and Dr Joe Gorski of the Naval Surface Warfare Center, Carderock Division for providing the CFD solution of the $Fr = 0.28$ case.

REFERENCES

1. Rhee SH, Stern F. Unsteady RANS method for surface ship boundary layer and wake and wave field. *International Journal for Numerical Methods in Fluids* 2001; **37**:445–478.
2. Weymouth G, Wilson R, Stern F. RANS CFD prediction of pitch and heave ship motions in head seas. *Journal of Ship Research* 2005; **49**(2):80–97.
3. Wilson R, Stern F, Coleman H, Paterson E. Comprehensive approach to verification and validation of CFD simulations—Part 2: Application for RANS simulation of a cargo/container ship. *Journal of Fluids Engineering* 2001; **123**(4):803–810.
4. Di Mascio A, Muscari R, Broglia R. Computation of free surface flows around ship hulls by a level set approach. *Proceedings of the 8th International Conference on Numerical Ship Hydrodynamics*, Busan, South Korea, 2003.
5. Broglia R, Di Mascio A, Muscari R. Numerical simulation of breaking waves around a wedge. *Proceedings of the 25th ONR Symposium on Naval Hydrodynamics*, St. John's Newfoundland and Labrador, Canada, 2004.
6. Carrica PM, Wilson RV, Stern F. Unsteady RANS simulation for the forward speed diffraction problem. *Computers and Fluids* 2006; **35**:545–570.
7. Dommermuth D, Sussman M, Beck R, O'Shea T, Wyatt D, Olson K, MacNeice P. The numerical simulation of ship waves using cartesian grid methods with adaptive mesh refinement. *Proceedings of the 25th ONR Symposium on Naval Hydrodynamics*, St. John's Newfoundland and Labrador, Canada, 2004.
8. Cura Hochbaum A, Vogt M. Towards the simulation of seakeeping and manoeuvring based on the computation of the free surface viscous ship flow. *Proceedings of the 24th ONR Symposium on Naval Hydrodynamics*, Fukuoka, Japan, 2002.
9. Duncan J. Spilling breakers. *Annual Review of Fluid Mechanics* 2001; **33**:519–547.
10. Rhee SH, Stern F. RANS modeling of spilling breaking waves. *Journal of Fluids Engineering* (ASME) 2002; **124**(2):424–432.
11. Muscari R, Di Mascio A. Simulation of naval flows with breaking waves. *Proceedings of the 8th International Conference on Numerical Ship Hydrodynamics*, Busan, South Korea, 2003.
12. Miyata H, Inui T. Nonlinear ship waves. *Advances in Applied Mechanics* 1984; **24**:215–288.
13. Dong R, Katz J, Huang T. On the structure of bow waves on a ship model. *Journal of Fluid Mechanics* 1997; **346**:77–115.
14. Olivieri A, Pistani F, Wilson R, Benedetti L, La Gala F, Campana E, Stern F. Froude number and scale effects and froude number 0.35 wave elevations and mean velocity measurements for bow and shoulder wave breaking of surface combatant DTMB 5415. *IIHR Hydroscience and Engineering Report No. 441*, IIHR Hydroscience and Engineering, The University of Iowa, Iowa City, IA, December 2004.
15. Carrica PM, Wilson RV, Stern F. An unsteady single-phase level set method for viscous free surface flows. *International Journal for Numerical Methods in Fluids* 2007; **53**(2):229–256.
16. Wilson R, Carrica P, Stern F. URANS simulations for a high-speed transom stern ship with breaking waves. *International Journal for CFD* 2006; **20**(2):105–125.
17. Menter FR. Two-equation Eddy viscosity turbulence models for engineering applications. *AIAA Journal* 1994; **32**:1598–1605.
18. Kang M, Fedkiw RP, Liu LD. A boundary condition capturing method for multiphase incompressible flow. *Journal of Scientific Computation* 2000; **15**:323–360.
19. Issa RI. Solution of the implicitly discretized fluid flow equations by operator splitting. *Journal of Computational Physics* 1985; **62**:40–65.
20. Suhs NE, Rogers SE, Dietz WE. PEGASUS 5: an automated pre-processor for overset-grid CFD. *AIAA Paper 2002-3186*; *AIAA Fluid Dynamics Conference*, St. Louis, MO, 2002.



DOI: 10.1002/fld

21. Balay S, Buschelman K, Gropp W, Kaushik D, Knepley M, Curfman L, Smith B, Zhang H. *PETSc User Manual*, ANL-95/11-Revision 2.1.5, Argonne National Laboratory, 2002.
22. Olivieri A, Pistani F, Campana E, Benedetti R, LaGala F, Wilson R, Stern F. Froude number and scale effects and Froude number 0.35 wave elevations and mean velocity measurements for bow and shoulder wave breaking of surface combatant DTMB 5415. *IIHR Report No. 441*, IIHR-Hydroscience and Engineering, The University of Iowa, 2004.
23. Stern F, Longo J, Penna R, Olivieri A, Ratcliffe T, Coleman H. International collaboration on Benchmark CFD validation data for surface combatant DTMB model 5415. *Proceedings of the 23rd ONR Symposium on Naval Hydrodynamics*, Val de Reuil, France, 2000.
24. Miller R, Gorski J, Wilson R, Carrica P. RANS simulation of a naval combatant using a single-phase level set method with overset grids. *Proceedings of the CFD Workshop Tokyo*, 2005.
25. Stern F, Wilson R, Coleman H, Paterson E. Comprehensive approach to verification and validation of CFD simulations—Part 1: Methodology and procedures. *Journal of Fluids Engineering* 2001; **123**(4):793–802.
26. Wilson R, Shao J, Stern F. Discussion: criticism of the 'correction factor' verification method [1]. *Journal of Fluids Engineering* 2004; **126**(4):704–706.
27. Stern F, Wilson R, Shao J. Quantitative V&V of CFD simulations and certification of CFD codes. *International Journal for Numerical Methods in Fluids* 2006; **50**(11):1335–1355.
28. Jordan S. A priori assessments of numerical uncertainty in large-Eddy simulations. *Journal of Fluids Engineering* (ASME) 2005; **127**:1171–1182.
29. Celik IB, Cehreli ZN, Yavuz I. Index of resolution quality for large Eddy simulations. *Journal of Fluids Engineering* (ASME) 2005; **127**:951–960.
30. Leroyer A, Hay A, Queutey P, Visonneau M. Free-surface RANSE simulations for moving bodies with adaptive mesh refinement. *Proceedings of the 5th Osaka Colloquium on Advanced Research on Ship Viscous Flow and Hull Form Design by EFD and CFD Approaches*, Osaka Prefecture University, Osaka, Japan, 2005.
31. Duncan J. The breaking and non-breaking wave resistance of a two-dimensional hydrofoil. *Journal of Fluid Mechanics* 1983; **126**:507–520.
32. Carrica P, Wilson R, Noack R, Xing T, Kandasamy M, Shao J, Sakamoto N, Stern F. A dynamic overset, single-phase level set approach for viscous ship flows and large amplitude motions and maneuvering. *Proceedings of the 26th Symposium on Naval Hydrodynamics*, Rome, Italy, 17–22 September 2006.
33. Wilson R, Carrica P, Stern F. Unsteady RANS method ship motions with application to roll for a surface combatant. *Computers and Fluids* 2006; **35**:501–524.



DOI: 10.1002/fld